Breaking Symmetries

Universal behaviour of asymmetric particles in confined Stokes flow

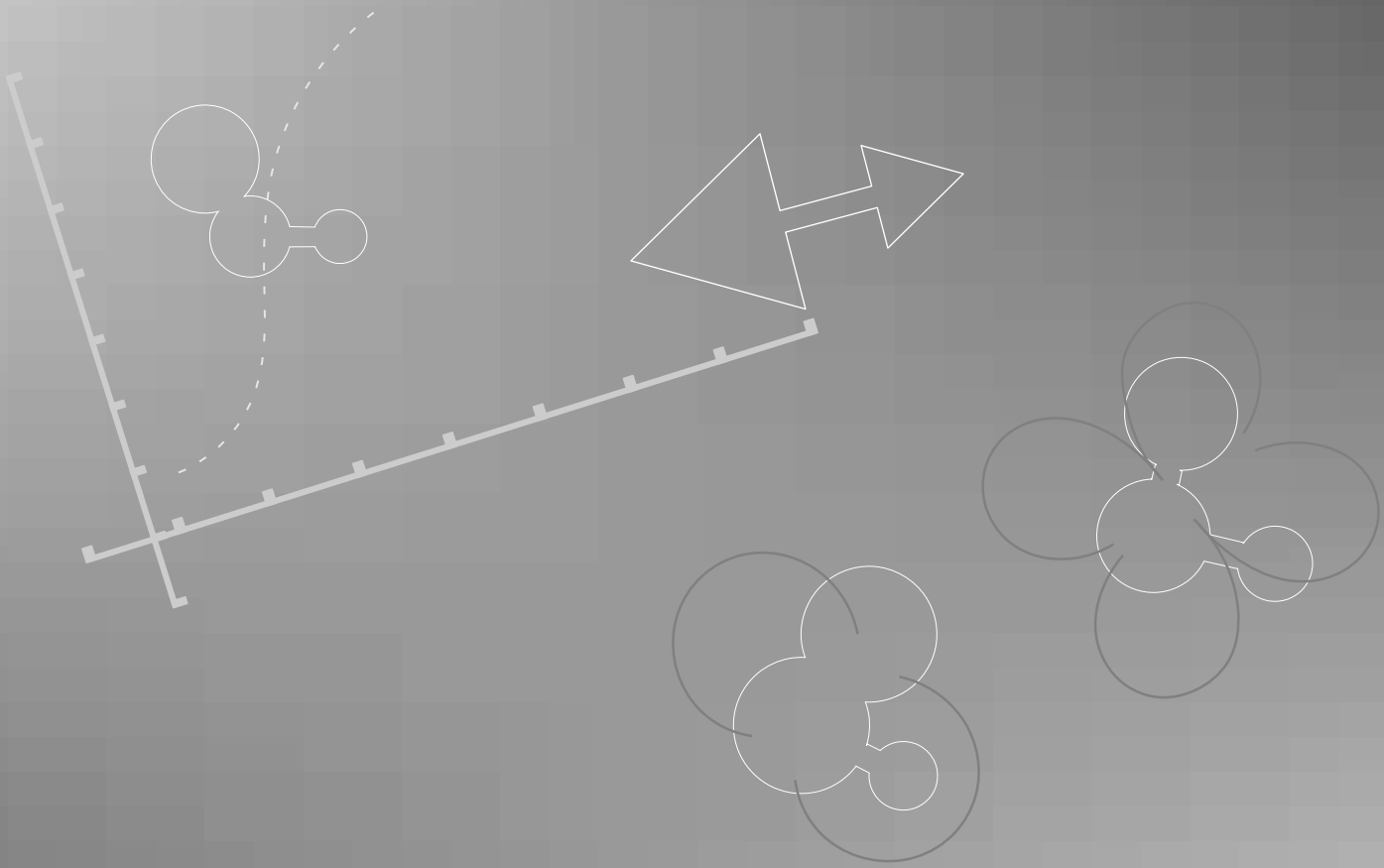

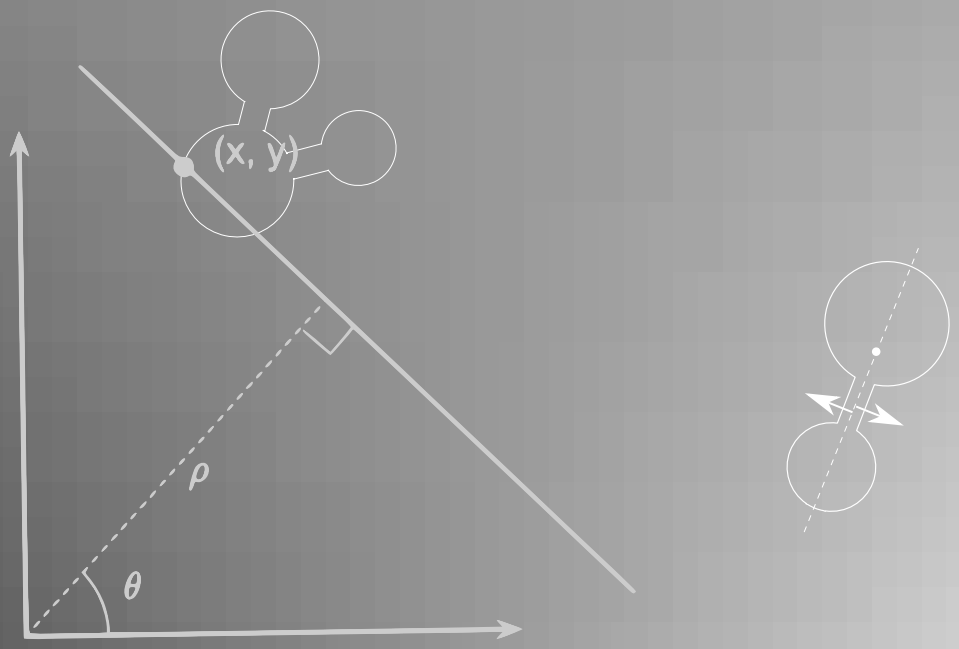

பிறப்பொக்கும் எல்லா உயிர்க்கும் சிறப்பொவ்வா
செய்தொழில் வேற்றுமை யான்.
(குறள் 972: பெருமை அதிகாரம்)

transliteration

piRappokkum ellA uyirkkum siRappovvA
seithozhil vERRumai yAn

-Thiruvalluvar

All beings are born equal. Distinction comes with differences in profession.

Breaking Symmetries

Universal Behaviour of Asymmetric Particles in Confined Stokes Flow

by

Nagaraj Nagalingam

in partial fulfillment of the requirements for the degree of

Master of Science
in Mechanical Engineering

at the Delft University of Technology,
to be defended publicly on Tuesday October 22, 2019 at 14:30 PM

Student number:	4750748	
Project duration:	November 16, 2018 – October 22, 2019	
Daily Supervisor:	Rumen Georgiev, Msc.	TU Delft
Thesis committee:	Prof. dr. ir. Johan T. Padding,	TU Delft, chairman
	Dr. H. Burak Eral,	TU Delft, supervisor
	Dr. Remco Hartkamp,	TU Delft

An electronic version of this thesis is available at `http://repository.tudelft.nl/`

TU Delft Delft University of Technology

Abstract

The recent advancements in lab-on-a-chip technologies has led to numerous studies on the collective dynamics of micro-particles suspended in a micro-fluidic channel. The role of hydrodynamics in "self-steering" of the particles in a low Reynolds flows is explicitly dependent only on the particle's exterior geometry. Thus richer responses can be achieved by controlling the transport and orientation of asymmetric particles under external flow.

In this work, we study the universal behaviour of particles with any arbitrary shape, strongly confined along direction involving height. The particle both translates and rotates in-plane, until a stable orientation is reached, after which it drifts cross-stream. By combining analytical, numerical and experimental techniques, we establish the generalised equations of motion for a particle sufficiently far away from the channel walls along width. Thus, the total motion of a particle is characterized by estimating only a few timescales, intrinsic to its exterior geometry. We discuss the shape properties defining the dynamics, and use them to derive an analytical framework. The results are then validated against the numerical solution utilizing an improved 2-Dimnesional Brinkman formulation for highly confined particles.

Experiments are performed using stop-flow lithography, where the dynamics of the photo-polymerized particles are observed by driving it out of equilibrium using an externally imposed pressure difference. We confirm the universal behaviour of the particles, except for a few cases, only when close to the stable orientation. Our experimentally observed rotational timescales consistently match the numerically computed values when multiplied by a factor of 1.8.

Keywords: microhydrodynamics, microfluidics, quasi-2D flow, confined Stokes flow, creeping flow, self-steering, microparticles.

Table of Contents

Notation

Regular Symbols	
$\mathbf{v}$	Local fluid velocity vector in 3D
p	Dynamic fluid pressure
$\mathbf{F}$	Hydrodynamic force on particle
$\mathbf{T}$	Hydrodynamic Torque on particle
$\mathbf{K}$	Translational resistance tensor
$\mathbf{\Omega}_O$	Rotational resistance tensor about O
$\mathbf{C}_O$	Coupling tensor about O
$\mathbf{I}$	Identity matrix
$\mathbf{Q}$	Transformation matrix
$\mathbf{X}$	Eigenvector matrix of dyadic
$\mathbf{D}$	Eigenvalue matrix of dyadic
$\mathbb{R}^0$	Resistance offered by a fixed particle in a streaming fluid
$\mathbb{R}'$	Resistance offered by an othetwise quiscent fluid to a moving particle
$\mathbb{R}^r$	Resistance tensor ratio ($\mathbb{R}'^{-1} \cdot \mathbb{R}^0$)
$\mathbf{B}(\mathbf{r})$	Mobility tensor in q2D
$\mathbf{M}$	Mobility tensor on particle surface in q2D
K_i	i^{th} eigenvalue of resistance dyadic
e_i	i^{th} eigenvector of resistance dyadic
e_{ij}	j^{th} component of i_{th} eigenvector
$\mathbf{U}$	Fluid velocity vector
$\mathbf{U}_\mathrm{p}$	Translational velocity of particle
U_0	Free stream velocity far away from particle
$\mathbf{u}$	Depth-averaged fluid velocity
$\mathbf{u}_\mathrm{max}$	Velocity found in the mid-plane of the Hele-Shaw cell
$\bar{\mathbf{u}}_\mathrm{p}$	Composite particle velocity
c	Characteristic particle dimension
l	Distance between the particles hydrodynamic centre and wall
d	diameter of the discs
h_g	Gap height
h_p	Particle height
b	Dimensionless gap height
H	Channel height
W	Channel width
$\mathbf{r}_{ab}$	Position of b with respect to a

Regular Symbols	
A	Area of a 2D particle
$d\mathbf{S}$	Elementary surface area vector over particle pointing towards fluid
S_p	Particle surface in 3D
q	An ansartz in z
Δt	Difference in time
$\dot{x}_\mathrm{p}, \dot{y}_\mathrm{p}$	Linear velocity of particle in (x, y)
$\hat{i}, \hat{j}, \hat{k}$	Unit vectors in fluid axes
$\hat{i}', \hat{j}', \hat{k}'$	Unit vectors in particle axes

Greek Symbols	
ρ	Fluid density
μ	dynamic viscosity of fluid
$\boldsymbol{\pi}$	Fluid stress tensor
$\dot{\theta}_\mathrm{p}$	angular velocity of particle along k
γ_c	Coefficient of friction due to channel
γ_p	Coefficient of friction in gaps on particle
δ	Dirac delta function
$\boldsymbol{\epsilon}$	isotropic triadic
$\mathbf{\Pi}$	Triadic stress field
ω	Scalar rotational velocity of the particle
$\boldsymbol{\omega}$	Vector rotational velocity of the particle
ζ	Frictional coefficient for fluid forces on particle
β	Transversal confinement ratio
ξ	Lateral confinement ratio
Ω_p	Particle domain in 2D
Γ_p	Particle boundary in 2D
Γ_w	Wall boundary in 2D
λ	Radius ratio of discs 2 and 3
κ	Radius ratio of discs 1 and 3
ϕ	angle in between the discs
Ξ	Parametric curve function of Ω_p

Subscript	
C	Centre of hydrodynamic stress
O	About arbitrary point O
∞	values in an infinite/unbound medium
l	On lateral side
t	On transversal side
eq	Equilibrium
seq	Stable equilibrium
x, y	x and y component of the force

Superscript	
$\dagger$	Matrix transpose
0	Effect due to fluid stream on a stationary particle
$'$	Effect of the moving particle in an otherwise quiescent fluid
$*$	Dimensionless values

Chapter 1

Introduction

Flow-mediated correlations play a crucial role in the dynamics of colloid suspensions[1]. In an ambient fluid at thermal equilibrium, large-scale dynamic structure can be formed through hydrodynamic interactions (HI's) arising from the motion of strongly correlated particles in a flow[2]. Inevitably, due to the wide range of applications in nature, the fluid flows in micro-channels have found their specific applications in the field of complex biological analysis[3]. The advent of lab-on-a-chip devices has led to simple fabrication technologies for the separation and sorting of cells, and flow cytometry[4]. In addition to the minimised use of reagents, the abundance and bio-friendly nature of the materials used for fabrication, such as PDMS and glass[5], has attracted the attention of process industries[6]. Through miniaturization of the process plant, state-of-the-art microfluidic technology has enabled the development of detailed manipulation of the micro-particles, such as, formation of one dimensional crystals[7] and elastic filaments in shear flows[8].

The theoretical framework for the hydrodynamic forces acting on a particle at small Reynolds number has been laid by Brenner and Happel[9]. The simplicity in the solution of Stokes equation has motivated the theoretical studies to traditionally focus on regular particle shapes such spheres and ellipsoids. In addition, for particles driven out of equilibrium due to externally imposed pressure difference within a Hele-Shaw cell, the long-ranged flow interactions are screened by the parallel confining walls. Consequently, due to the momentum screening, two-body interactions can be studied to explain the behaviour of colloids up to certain particle densities[10]. Recently, Uspal et al.[11] conducted both numerical and experimental study on the self-steering ability of dumbbell-shaped particles with one plane of symmetry in a confined microchannels subjected to creeping flow. The driving of more asymmetric objects generally includes coupling between translation and rotation — object rotates when subjected to a force and, conversely, translates when under torque. Such richer responses can be harnessed to obtain steerable colloids — microscopic shapes whose transport and orientation can be controlled to a higher degree.

In this work, we focus on the general behaviour of isolated asymmetric objects in a confined Stokes flow, and the resulting effect of hydrodynamic forces on their orientational alignment. We derive an universal behaviour for any arbitrary shape of the particles as it both translates and rotates within a viscous medium at sufficient distance from the laterally (along horizontal) bounding walls. The present work showcases this phenomenon both numerically and experimentally. In addition, the numerical model is supported by an analytical framework through which we derive general equations of motion for an arbitrary shape. Experimentally, the particles are produced using stop-flow lithography (SFL) in a shallow microfluidic device. The behaviour of the particle is observed and recorded using an optical microscope, and image processed using Circular Hough Transform. The fundamental shapes under consideration are developed by assembling three discs (see fig. 1.1), with the asymmetry controlled by changing the disc radius ratios and their angular positions.

We begin by discussing in chapter 2 the general theory behind the intrinsic hydrodynamic resistance of an arbitrary body in an unconfined, unbound flow domain, and extend it to Quasi-2D channels. In chapter 3, we introduce the model formulation and establish our own numerical method followed by experimental technique. In chapter 4, we begin by comparing our numerical model to the existing methods. Further, we derive general

equations of motion from the analytical model utilizing the properties of the resistance tensors and validate it against both the computational and experimental results. Finally, in chapter 5, we summarise our results and provide recommendations.

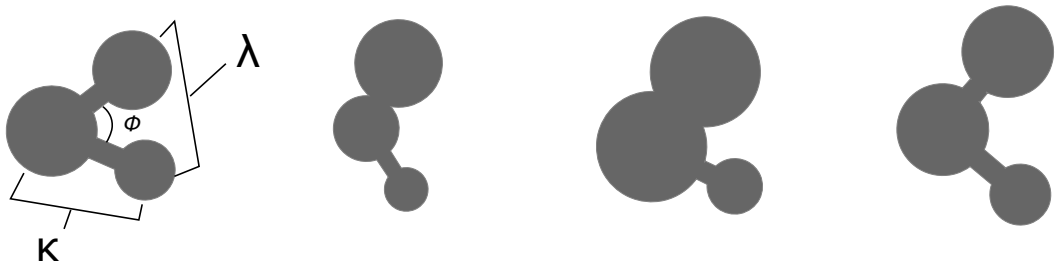

Figure 1.1: Sample particle geometries under consideration. Different particle shapes are produced by varying the disc radius ratios - λ and κ, and the angle between them - ϕ.

Chapter 2

Theory

2.1 Stokes Flow

At small Reynolds numbers for unsteady flows, the kinematic and dynamic equations of motion of a incompressible, viscous fluid are, respectively,

$$\boldsymbol{\nabla} \cdot \mathbf{v} = 0 \tag{2.1}$$

$$\rho \partial_t \mathbf{v} + \boldsymbol{\nabla} p = \mu \nabla^2 \mathbf{v}, \tag{2.2}$$

in which $\mathbf{v}$ is the local fluid velocity, p the pressure, ρ the fluid density and μ the dynamic viscosity. The fluid is considered isotropic and isothermal with no external forcing.

Since we deal only with the steady flows, the temporal term will be ignored anyway in comparison to the viscous terms due to overdamping. This approximation holds as long as the dimensionless group, $\rho c^2/(\mu T)$, is small (c and T are some characteristic dimension and time respectively), known as the creeping flow limit. The *quasi-static* equation of motion is therefore taken to be

$$\boldsymbol{\nabla} p = \mu \nabla^2 \mathbf{v} \tag{2.3}$$

even for unsteady equations.

The force on an arbitrary particle in a streaming flow of viscous fluid is uniquely determined by the exterior geometry, the particle orientation and its relative distance to the walls. The stresses set up at the surface of a rigid particle of arbitrary shape moving through a fluid with net flow can be integrated to calculate the force $\mathbf{F}$ and torque $\mathbf{T}$. Considering a particle suspended in a moving fluid, the hydrodynamic force and torque can be represented as

$$\mathbf{F} = \iint_{S_p} \boldsymbol{\pi} \cdot d\mathbf{S} \tag{2.4}$$

and

$$\mathbf{T} = \iint_{S_p} \mathbf{r} \times (\boldsymbol{\pi} \cdot d\mathbf{S}), \tag{2.5}$$

where S_p denotes the surface of the particle, $d\mathbf{S}$ is an elemental vector normal to the surface area pointing towards fluid volume and $\boldsymbol{\pi}$ is the stress tensor. For a Newtonian, incompressible fluid this symmetric tensor is given by the expression,

$$\boldsymbol{\pi} = -\mathbf{I}p + \mu(\boldsymbol{\nabla}\mathbf{v} + \boldsymbol{\nabla}\mathbf{v}^\dagger), \tag{2.6}$$

where $\mathbf{I}$ is the identity matrix and $\boldsymbol{\nabla}\mathbf{v}^\dagger$ is the transpose (conjugate) of $\boldsymbol{\nabla}\mathbf{v}$.

An object in three-dimensional space will have in total 6 kinetic degrees of freedoms: three for translational and three for rotational motion along the orthogonal triad of unit vectors $(\hat{i}, \hat{j}, \hat{k})$, respectively.

2.1.1 Translating Particle

Let $\mathbf{U}$ be an arbitrary fluid velocity conforming to eqs. (2.1) and (2.3). By imposing a no-slip boundary condition on the particle surface, it thereby satisfies the boundary conditions.

$$\mathbf{U} = \mathbf{U}_\mathrm{p} \quad \text{on} \quad S_\mathrm{p} \tag{2.7}$$

Using the Lorentz reciprocal theorem, we can prove the following equality for any two arbitrary, distinct velocity fields and the corresponding stresses over the particle: $(\grave{\mathbf{v}}, \grave{\boldsymbol{\pi}})$ and $(\grave{\grave{\mathbf{v}}}, \grave{\grave{\boldsymbol{\pi}}})$,

$$\grave{\grave{\mathbf{U}}} \cdot \grave{\mathbf{F}} = \grave{\mathbf{U}} \cdot \grave{\grave{\mathbf{F}}}, \tag{2.8}$$

which implies a linear relation of $\mathbf{F}$ to $\mathbf{U}$ (Supplementary Information A). Consequently, the more general form is therefore

$$\mathbf{F} = \mu \mathbf{K} \cdot \mathbf{U}, \tag{2.9}$$

where $\mathbf{K}$ is a second-rank symmetric tensor, known as the *translational tensor*[12]. It characterizes the resistance of an arbitrary body to translational motion at small Reynolds numbers, and has the dimensions of length. It is an intrinsic property of the body depending solely on its external configuration. Thus, it is independent of the properties or velocity of the fluid.

For a particle moving in response to the streaming flow, due to the linearity in the Stokes flow and complying to *Galilean invariance*, the net force on the particle in an unbounded medium can be represented as

$$\mathbf{F} = \mu \mathbf{K} \cdot (\mathbf{U}_0 - \mathbf{U}_\mathrm{p}) = \mathbf{F}^0 + \mathbf{F}', \tag{2.10}$$

where $\mathbf{U}_0$ is the free stream velocity of the fluid far away from the particle. $\mathbf{F}^0$ and $\mathbf{F}'$ are the frictional forces acting on the particle due to fluid stream and particle motion respectively. Therefore, the instantaneous rate of mechanical energy dissipation is $\mathbf{F} \cdot \mathbf{U}_\mathrm{p}$.

As a consequence of the properties of symmetric tensors, the three eigenvalues, $K_i (i = 1, 2, 3)$, of the characteristic equation

$$\|\mathbf{K} - K\mathbf{I}\| = 0 \tag{2.11}$$

are real, with three mutually perpendicular eigenvectors, $e_i (i = 1, 2, 3)$. Moreover, these eigenvalues are positive, and are referred to as the *principal resistances*. Thus, every arbitrary particle must possess at least three mutually perpendicular axes known as *principal axes of resistance*, such that if it is moving parallel to one of them it will experience a force only in that direction.

2.1.2 Rotating Particle

Analogous to the translating particle, an arbitrary particle in a otherwise quiescent fluid experiences a torque, $\mathbf{T}$, due to its rotation $\boldsymbol{\omega}$. The no slip condition at the surface of the rotating particle requires that

$$\mathbf{v} = \boldsymbol{\omega} \times \mathbf{r} \quad \text{on} \quad S_\mathrm{p}, \tag{2.12}$$

in which $\mathbf{r}$ is measured from any point lying on the axis of rotation. Similar to the translational case the linear dependence of torque about an arbitrary point, O, to the angular velocity can be proved using the reciprocal relation. Arguments similar to those of section 2.1.1 thereby lead to the relation

$$\mathbf{T} = -\mu \boldsymbol{\Omega} \cdot \boldsymbol{\omega}, \tag{2.13}$$

where $\boldsymbol{\Omega}$ is a second-rank symmetric, positive definite tensor, termed as *rotation tensor* about point O. Its dimensions are those of a length cubed and has three principal resistances along mutually perpendicular directions. In contrast to the translational tensor, the rotation tensor is a function of position, O, thereby taking different values at different points.

2.1.3 Coupling Tensor

Let $\grave{\mathbf{v}}$ and $\grave{\grave{\mathbf{v}}}$ respectively be two distinct fluid velocity fields induced by steady translation and rotation of a particle through a stationary fluid (the single and double reverse primes refer, respectively, to translational and rotational fields). The force and torque experienced by the particle in consequence of its translation is

$$\grave{\mathbf{F}}_O = \mu \iint_{S_p} d\mathbf{S} \cdot \grave{\mathbf{\Pi}} \cdot \grave{\mathbf{U}}_O \tag{2.14}$$

$$\grave{\mathbf{T}}_O = \mu \iint_{S_p} \mathbf{r}_O \times (d\mathbf{S} \cdot \grave{\mathbf{\Pi}}) \cdot \grave{\mathbf{U}}_O, \tag{2.15}$$

where $\mathbf{\Pi}$ is a triadic stress field existing due to the linearity in the governing equation, such that $\boldsymbol{\pi} = \mu\mathbf{\Pi} \cdot \mathbf{U}$. $\mathbf{U}_O$ is the linear velocity at point O calculated with respect to *instantaneous axis of rotation* of the particle. If we define the constant dyadics

$$\mathbf{K} = -\iint_{S_p} d\mathbf{S} \cdot \grave{\mathbf{\Pi}}, \quad \mathbf{C}_O = \iint_{S_p} \mathbf{r}_O \times (d\mathbf{S} \cdot \grave{\mathbf{\Pi}}) \tag{2.16a, 2.16b}$$

eqs. (2.14) and (2.15) become

$$\grave{\mathbf{F}}_O = -\mu\mathbf{K} \cdot \grave{\mathbf{U}}_O \tag{2.17}$$

$$\grave{\mathbf{T}}_O = -\mu\mathbf{C}_O \cdot \grave{\mathbf{U}}_O \tag{2.18}$$

We name $\mathbf{C}_O$ the *coupling tensor*[13] at O, which couples the torque on a particle to its linear motion. Like rotational tensor $\mathbf{C}_O$ depends only on the exterior geometry of the particle and the position of O, while the coupling tensor is not generally symmetric. In similar fashion, the force and hydrodynamic torque about O, which the particle experiences by virtue of its rotation are respectively,

$$\grave{\grave{\mathbf{F}}}_O = -\mu\mathbf{C}_O^\dagger \cdot \boldsymbol{\omega} \tag{2.19}$$

$$\grave{\grave{\mathbf{T}}}_O = -\mu\mathbf{\Omega}_O \cdot \boldsymbol{\omega} \tag{2.20}$$

The total force experienced by the particle in result of its combined translational and rotational motion is

$$\mathbf{F} = \grave{\mathbf{F}}_O + \grave{\grave{\mathbf{F}}}_O = -\mu(\mathbf{K} \cdot \grave{\mathbf{U}}_O + \mathbf{C}_O^\dagger \cdot \boldsymbol{\omega}) \tag{2.21}$$

while the total torque about O is

$$\mathbf{T}_O = \grave{\mathbf{T}}_O + \grave{\grave{\mathbf{T}}}_O = -\mu(\mathbf{C}_O \cdot \grave{\mathbf{U}}_O + \mathbf{\Omega}_O \cdot \boldsymbol{\omega}) \tag{2.22}$$

2.1.4 Centre of Reaction

Consequently, about a point, eqs. (2.21) and (2.22) may be written in terms of partitioned matrices as follows:

$$\begin{pmatrix} \mathbf{F} \\ \mathbf{T}_O \end{pmatrix} = -\mu \begin{pmatrix} \mathbf{K} & \mathbf{C}_O^\dagger \\ \mathbf{C}_O & \mathbf{\Omega}_O \end{pmatrix} \cdot \begin{pmatrix} \mathbf{U}_O \\ \boldsymbol{\omega} \end{pmatrix} \tag{2.23}$$

It is logical to refer to the 6 x 6 square matrix appearing above as the *resistance tensor* ($\mathbb{R}$). As a consequence of the symmetry of its submatrices $\mathbf{K}$ and $\mathbf{\Omega}_O$, $\mathbb{R}$ is symmetric with six real eigenvalues. In addition, the resistance matrix is positive-definite at all points O. Thus a complete characterization of the hydrodynamic resistance of rigid body to translational and rotational motions in Stokes flow requires the knowledge of three fundamental tensors. Moreover, this number can be reduced by the nature of geometric symmetry possessed by the particle.

Every particle, irrespective of shape, possesses a unique, intrinsic geometrical point at which $\mathbf{C}_O$ is symmetric. This point is termed as *centre of hydrodynamic reaction*, denoted by symbol R. The exact location of this point from any point of interest (O) is found to be,

$$\mathbf{r}_{OR} = [(\mathbf{I} : \mathbf{K})\mathbf{I} - \mathbf{K}]^{-1} \cdot \epsilon : \mathbf{C}_O, \tag{2.24}$$

in which ϵ is an isotropic triadic. A special case where the translational and rotational motions are *decoupled* ($\mathbf{C}_R = 0$), the centre of reaction becomes the *centre of hydrodynamic stress* (C). The latter being the centre of fluid stress resulting from the relative translational motion of particle and fluid. The couple of the hydrodynamic force about C is therefore zero, by definition. Conversely, a body rotating in a quiescent fluid about any axis which contains this point will experience no hydrodynamic force.

2.2 Quasi 2-D Flow

2.2.1 Brinkman Equation

Now we consider the fluid to be suspended between two parallel plates that are very close to each other, separated by a height H along $\hat{z}$. In $\hat{y}$ the channel is bounded by two side walls at a distance of W(width) from each other. Let the fluid be driven by external pressure along $\hat{x}$. The flow in between the confinement, far from channel side walls or suspended particles, takes a parabolic form along the height (see fig. 2.1), represented using a Hele-Shaw channel as

$$\mathbf{v} = \mathbf{u}_{\max}(x, y)\frac{4z(H - z)}{H^2} \tag{2.25}$$

where, $z = H/2$, is the position of the midplane and $\mathbf{u}_{\max}(x, y)$ is the velocity at $(x, y, H/2)$.

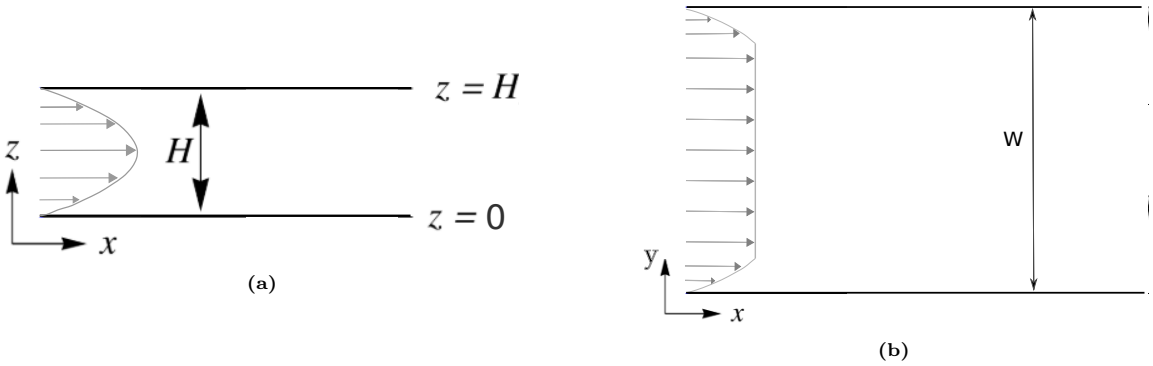

Figure 2.1: Flow within a Hele-Shaw channel. (**a**) Side view of the channel displaying the parabolic velocity profile (**b**) Top view of the channel representing the uniform flow between the lateral/horizontal walls. (source [14])

By exploiting the disparity between two length scales, $H \ll W$, it is safe to approximate pressure, p, as a strict function of x and y. Substituting eq. (2.25) into eq. (2.3), we obtain

$$-\boldsymbol{\nabla} p + \mu\frac{4z(H - z)}{H^2}\nabla^2_{\mathrm{2D}}\mathbf{u}_{\max} - \left(\frac{8\mu}{H^2}\right)\mathbf{u}_{\max} = 0, \tag{2.26}$$

in which $\nabla^2_{2D} = {\partial_x}^2 + {\partial_y}^2$. We define $\mathbf{u}(x, y)$ as the depth averaged fluid velocity, where $\mathbf{u} = 2\mathbf{u}_{\max}/3$. Further, we remove the z dependence in eq. (2.26) by averaging it over channel depth H

$$-\boldsymbol{\nabla} p + \mu\nabla^2_{\mathrm{2D}}\mathbf{u} - \left(\frac{12\mu}{H^2}\right)\mathbf{u} = 0 \tag{2.27}$$

Multiplying the above equation by H, we obtain the *two-dimensional* Brinkman equation

$$-\boldsymbol{\nabla} p_{2D} + \mu H\nabla^2_{\mathrm{2D}}\mathbf{u} - \left(\frac{12\mu}{H}\right)\mathbf{u} = 0, \tag{2.28}$$

where $p_{2D} \equiv p(x,y)H$ and $\mu_{2D} \equiv \mu H$ denote the two-dimensional pressure field and dynamic viscosity, respectively. Interestingly eq. (2.28) has an additional third term to the conventional two-dimensional Stokes equation. This term represents the friction exerted by the confinement on the fluid and violates the Galilean invariance principle.

2.2.2 Violation of Galilean Invariance

Here we consider a simple problem in two dimensions where an arbitrary particle spans the complete channel height. Let the particle move with a velocity $\mathbf{U}_p$ when subjected to a uniform external flow field $\mathbf{U}_0$. The fluid obeys no-slip and no-penetration conditions on the solid boundaries. A simplified model for the drag force, $\mathbf{F}_{2D}$, on the particle is[15]

$$\mathbf{F}_{2D} = \zeta(\mathbf{U}_0 - \mathbf{U}_p) + A\left(\frac{12\mu}{H}\right)\mathbf{U}_0, \tag{2.29}$$

in which ζ is a drag/frictional coefficient and A in the area of the 2D particle. The additional force due to the second term present in the right hand side of the above equation contributes to the violation of Galilean variance, and is linearly dependent on stream velocity.

2.2.3 Confined Rigid Bodies

Now let the particle have lubrication layers separating it from the confining plates along $\hat{z}$ (fig. 2.2). Since these thin gaps are not modelled by the 2D Brinkman equation, the forces due to them are not included in $\mathbf{F}_{2D}$. We consider the complete set of forces on the particle, including from the lubricating gaps. Due to the over-damped nature of the system, at any instant in time, the force and torque on the particle must vanish (here we assume that all non-hydrodynamic forces are absent)

$$\zeta(\mathbf{U}_0 - \mathbf{U}_p) + A\left(\frac{12\mu}{H}\right)\mathbf{U}_0 - A\left(\frac{2\mu}{h_g}\right)\mathbf{U}_p = 0 \tag{2.30}$$

Above we have applied Couette flow in the two thin lubricating gaps, each of height, h_g, that separate the particle from the confining plates. We define the coefficients of friction due to channel and particle as $\gamma_c \equiv A\,(12\mu/H)$ and $\gamma_p \equiv A\,(2\mu/h_g)$, and rearrange eq. (2.30)

$$(\zeta + \gamma_c)\mathbf{U}_0 - (\zeta + \gamma_p)\mathbf{U}_p = 0 \tag{2.31}$$

The above equation, however, is only valid for extremely confined particles - the hydraulic resistance within the gaps are high compared to the ones inbetween the confinement on particle sides. When the particle is less confined, Poiseuille flow needs to be implemented in the gaps resulting from pressure variations across particle. Thus, this introduces two additional coefficients γ_0' and γ_p' due to the fluid stream and particle motion, respectively. Adding these terms to the existing coefficients contribute to pure Poiseuille flow (γ_0') due to $\mathbf{U}_0$ and hybrid flow ($\gamma_p + \gamma_p'$) due to $\mathbf{U}_p$ in the gaps. The corrected dynamic equation for the particle is as follows,

$$(\zeta + \gamma_c + \gamma_0')\mathbf{U}_0 - (\zeta + \gamma_p + \gamma_p')\mathbf{U}_p = 0 \tag{2.32}$$

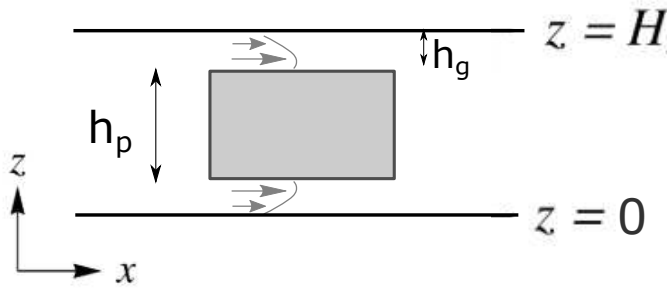

Figure 2.2: Confined particle in Q2D. Figure showing the description of the particle height, h_p, and gap heights, h_g. In addition, it also displays a hybrid flow in the lubrication gaps.

2.2.4 Resistance Tensors in Q2D

In a q2D system since the kinematic degrees of freedom are restricted in major directions - the particle translates in plane (x, y) with velocity $\mathbf{U}$ and rotates about z with angular velocity ω. Correspondingly, the resistance tensor ($\mathbb{R}$) simplifies to a 3×3 matrix. Therefore, a suspended particle experiences an in-plane force $\mathbf{F}_{x,y}$, and torque $\mathbf{T}_z$ normal to the plane. Henceforth throughout this report we restrict ourselves to a q2D system.

The force $\mathbf{F}$, being a linear vector function of velocity, it can effectively be decomposed into the solution to the fixed particle subjected to an external flow, $f_1(\mathbf{U}_0)$, and the solution to the moving particle in a quiescent fluid, $f_2(\mathbf{U}_\mathrm{p})$,

$$\mathbf{F} = f(\mathbf{U}_0, \mathbf{U}_\mathrm{p}) = f_1(\mathbf{U}_0) + f_2(\mathbf{U}_\mathrm{p}) \tag{2.33}$$

In eq. (2.32) we have essentially grouped the forces as: (i) due to an imposed external flow, and (ii) due to particle's motion. The effective drag coefficients for $\mathbf{U}_0$ and $\mathbf{U}_\mathrm{p}$ are *not equal*. Thus for a quasi-2D system, by extending the relations of linear forces to couples, the resistance tensor can ably be represented into two distinct forms: (i) the resistance offered by a fixed particle subjected to a streaming flow - $\mathbb{R}^0$ and (ii) the resistance to a moving particle offered by fluid otherwise at rest - $\mathbb{R}'$. Thus, the force contributions on the particle at any instant in time must obey

$$\begin{pmatrix} \mathbf{F} \\ \mathbf{T} \end{pmatrix} = \mu\mathbb{R}^0 \cdot \mathbf{U}_0 - \mu\mathbb{R}' \cdot \begin{pmatrix} \mathbf{U}_p \\ \boldsymbol{\omega} \end{pmatrix} = \begin{pmatrix} 0 \\ 0 \end{pmatrix}, \tag{2.34}$$

where $\mathbb{R}^0$ is a 3×2 matrix, and

$$\mathbb{R}^r = \mathbb{R}'^{-1} \cdot \mathbb{R}^0$$

2.2.5 Transformation of Resistance Tensor

Let $\mathbf{X}$ and $\mathbf{D}$ respectively be the matrices composed of eigenvectors and eigenvalues of a given translational resistance tensor $\mathbf{K}$. The solution to the equation

$$\mathbf{K} \cdot \mathbf{X} = \mathbf{X} \cdot \mathbf{D} \tag{2.35}$$

relates each of the eigenvectors represented using the unit vectors $(\hat{i}, \hat{j})$; affixed to the fluid coordinates. Therefore, we write

$$\mathbf{e}_i = e_{i1}\hat{i} + e_{j2}\hat{j} \tag{2.36}$$

the components (e_{i1}, e_{i2}), for each i, correspond to its respective eigenvector. The resistance tensor, thus, is governed by the equation

$$\mathbf{K} \cdot \mathbf{e}_i = k_i \mathbf{e}_i \tag{2.37}$$

In simple terms, if $(\hat{i}', \hat{j}')$ are the *normalized eigenvectors* represented in the particle's coordinate system, then the resistance dyadic can be expressed in the symmetric (binomial) form

$$\mathbf{K} = K_1\hat{i}'\hat{i}' + K_2\hat{j}'\hat{j}', \tag{2.38}$$

where each component $(K_i\{i = 1, 2, 3\})$ is the eigenvalue $(\mathbf{D})$ of the tensor $\mathbf{K}$. Conversely, for a particle symmetrically confined along z and *unbound* along y, this binomial form of the translational tensor can be transformed from the particle's reference frame to fluid's coordinates.

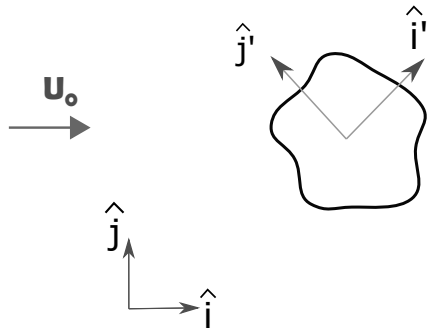

Figure 2.3: Different frames of reference. Image represents the particle frame $(\hat{i}', \hat{j}')$ with respect to the fluid frame of reference $(\hat{i}, \hat{j})$. The x-axis of the fluid coordinate is always aligned with the flow.

The principal resistances (D_1, D_2) of the particle are known. The translational resistance tensor of the same particle with respect to the fluid coordinate system is

$$\mathbf{K} = \mathbf{X} \cdot \mathbf{D} \cdot \mathbf{X}^{-1} \tag{2.39}$$

This transformation can be extended to determine the translation tensor in fluid reference frame, ${}^{f}\mathbf{K}$, even when the tensor is known for any arbitrary coordinate frame positioned at an angle, $-\theta$, to the fluid frame. Here we consider only the *angular transformation* since $\mathbf{K}$ is independent of the point of interest. Let $\mathbf{Q}$ be the transformation matrix

$$\mathbf{Q} = \begin{pmatrix} \cos\theta & -\sin\theta \\ \sin\theta & \cos\theta \end{pmatrix} \tag{2.40}$$

Then

$${}^{f}\mathbf{K} = \mathbf{Q} \cdot {}^{\theta}\mathbf{K} \cdot \mathbf{Q}^{-1}, \tag{2.41}$$

where ${}^{\theta}\mathbf{K}$ is the tensor value in the known frame. Since $\mathbf{Q}$ is an orthogonal matrix, $\mathbf{Q}^{-1} = \mathbf{Q}^{\dagger}$. Hence,

$${}^{f}\mathbf{K} = \mathbf{Q} \cdot {}^{\theta}\mathbf{K} \cdot \mathbf{Q}^{\dagger} \tag{2.42}$$

Although these transformation laws are applicable to the rotational tensor, in our system of interest (q2D), the $\mathbf{\Omega}$ is a scalar. However, *linear transformations* affect the rotational tensor since it is point dependent. Similarly, the coupling tensor ($\mathbf{C}$), which is a 2D vector (for q2D) in space, undergoes both angular and linear transformation as it is subjective to the point of consideration.

Using eq. (2.16), we determine the manner in which $\mathbf{C}$ varies with position. For any point P affixed to the particle,

$$\mathbf{C}_P = \iint_{S_p} \mathbf{r}_P \times (d\mathbf{S} \cdot \mathbf{\Pi}) \tag{2.43}$$

Upon subtracting eq. (2.16b) from the above and applying eq. (2.16a) we arrive at

$$\mathbf{C}_P = \mathbf{C}_O - \mathbf{r}_{OP} \times \mathbf{K}, \tag{2.44}$$

where $\mathbf{r}_{OP}$ is the position vector of P relative to O. Equation (2.44) gives the rule by which the coupling tensor transforms from point to point. Furthermore, since $\mathbf{K}$ is symmetric, it follows that

$$\mathbf{C}_P^{\dagger} = \mathbf{C}_O^{\dagger} - \mathbf{K} \times \mathbf{r}_{OP} \tag{2.45}$$

By the same means we can obtain the rule by which the rotation tensor transforms from point to point. For an arbitrarily moving particle,

$$\mathbf{T}_O = \iint_{S_p} \mathbf{r}_O \times (d\mathbf{S} \cdot \boldsymbol{\pi}) \tag{2.46}$$

and

$$\mathbf{T}_P = \iint_{S_p} \mathbf{r}_P \times (d\mathbf{S} \cdot \boldsymbol{\pi}) \tag{2.47}$$

we note that $\boldsymbol{\pi}$ is the stress tensor arising from the combined translational and rotational motion, and is independent of the point of interest. Upon subtracting the latter equations we obtain

$$\mathbf{T}_O - \mathbf{T}_P = \mathbf{r}_{OP} \times \mathbf{F} \tag{2.48}$$

in which

$$\mathbf{F} = \iint_{S_p} (d\mathbf{S} \cdot \boldsymbol{\pi})$$

is the hydrodynamic force on the rigid body. $\mathbf{F}$ and $\mathbf{T}_O$ are given by eqs. (2.21) and (2.22) respectively, and $\mathbf{T}_P$ by the equation of the form eq. (2.22). When these are substituted into eq. (2.48) one obtains

$$-\mu(\mathbf{C}_O \cdot \mathbf{U}_O - \mathbf{C}_P \cdot \mathbf{U}_P) - \mu(\boldsymbol{\Omega}_O - \boldsymbol{\Omega}_P) \cdot \omega = -\mu\, \mathbf{r}_{OP} \times (\mathbf{K} \cdot \mathbf{U}_O + \mathbf{C}_O^{\dagger} \cdot \omega) \tag{2.49}$$

$\mathbf{C}_P$ in this equation may be eliminated via eq. (2.44). Using the kinematics for rigid body motions, the linear velocities of O and P are linked by the relation $\mathbf{U}_O = \mathbf{U}_P + \mathbf{r}_{OP} \times \omega$. Considering the fact that $\boldsymbol{\Omega}$ is an arbitrary vector - need not be rotating about an axis through O, and utilizing some elementary identities to simplify the resulting expression, we ultimately obtain

$$\boldsymbol{\Omega}_P = \boldsymbol{\Omega}_O - \mathbf{r}_{OP} \times \mathbf{K} \times \mathbf{r}_{OP} + \mathbf{C}_O \times \mathbf{r}_{OP} - \mathbf{r}_{OP} \times \mathbf{C}_O^{\dagger} \tag{2.50}$$

Equations (2.44) and (2.50) exhibit the property of linear transformation of $\mathbf{C}$ and $\boldsymbol{\Omega}$, while the angular transformation can be explained analogous to that of $\mathbf{K}$. Conclusively, about a point, the transformation of the resistance tensor can be represented as

$${}^{f}\mathbb{R} = \begin{pmatrix} \mathbf{Q} \cdot {}^{\theta}\mathbf{K} \cdot \mathbf{Q}^{\dagger} & \mathbf{Q} \cdot {}^{\theta}\mathbf{C}^{\dagger} \\ (\mathbf{Q} \cdot {}^{\theta}\mathbf{C}^{\dagger})^{\dagger} & \boldsymbol{\Omega} \end{pmatrix} \tag{2.51}$$

2.3 Effect of Finite Boundaries on the Stokes Resistance

2.3.1 Mobility Tensor

The fluid motion generated at large distances from any finite body in an unbounded fluid must be identical to that which would result when the body is replaced by a point force of equal strength, situated at its centre of hydrodynamic stress. At such vast distances the explicit shape of the particle is clearly irrelevant. The velocity field due to a force monopole, $\mathbf{f}(\mathbf{r}) = \mathbf{F}\,\delta(\mathbf{r})$, for a point positioned at $\mathbf{r}$ from the centre in a q2D channel is

$$\mathbf{u}(\mathbf{r}) = \mathbf{B}(\mathbf{r}) \cdot \mathbf{F}, \tag{2.52}$$

in which, $\mathbf{B}(\mathbf{r})$, the *mobility tensor* is independent of the size and shape of the particle. It has the value [16]

$$\mathbf{B}(\mathbf{r}) = -\alpha(h/H)\, \frac{H}{\mu r^2}(\mathbf{I} - 2\frac{\mathbf{r} \otimes \mathbf{r}}{r^2}), \tag{2.53}$$

where $\alpha(h_\mathrm{p}/H)$ is a dimensionless prefactor depending on the confinement ratio h_p/H, with h_p being the particle height. Let $\mathbf{M}$ be the value of mobility tensor at the points on the particle surface, $\mathbf{r}_\mathrm{p}$, such that

$$\mathbf{M} = \mathbf{B}(\mathbf{r}_\mathrm{p}) \tag{2.54}$$

Thus $\mathbf{M}$ corresponds to the inverse of the translational tensor for a particle with velocity, $\mathbf{U}_\mathrm{p} = \mathbf{u}(\mathbf{r}_\mathrm{p})$,

$$\mathbf{u}(\mathbf{r}_\mathrm{p}) = \mathbf{K}^{-1} \cdot \mathbf{F} = \mathbf{M} \cdot \mathbf{F} \tag{2.55}$$

2.3.2 Method of Reflexions

Using the knowledge of the Method of Reflections developed by Cox and Brenner[17,18], we derive our own equation for a q2D system. Only for this section the translational and rotational resistance tensor would correspond to the forces acting on the particle sides. Thus, we do not consider the forces in the gaps since the disturbances analysed are reflecting between the lateral walls (along width) and 2D particle boundary Γ_p.

2.3.2.1 Translation

For the equations of motion eqs. (2.1) and (2.3), we impose the following conditions on particle (Γ_p) and wall (Γ_w) boundaries.

$$\mathbf{u} = \mathbf{U}_\mathrm{p} \quad \text{on } \Gamma_\mathrm{p} \quad \text{and} \quad \mathbf{u} = 0 \quad \text{on } \Gamma_\mathrm{w} \tag{2.56}$$

As the governing equations and boundary conditions are linear, we can effectively decompose fluid velocity and pressure into a sum of fields

$$\mathbf{v} = \mathbf{v}^{(1)} + \mathbf{v}^{(2)} + \mathbf{v}^{(3)} + \mathbf{v}^{(4)} + ..., \tag{2.57}$$

$$p = p^{(1)} + p^{(2)} + p^{(3)} + p^{(4)} + ..., \tag{2.58}$$

each term, $(\mathbf{v}^{(n)}, p^{(n)})$, separately satisfies the governing differential equation. For a system satisfying the boundary condition eq. (2.56), the individual fields are to be computed successively by utilization of the following boundary-value problem

$$\mathbf{u}^{(1)} = \mathbf{U}_\mathrm{p} \quad \text{on} \quad \Gamma_\mathrm{p}, \tag{2.59}$$

$$\mathbf{u}^{(2)} = -\mathbf{K}^r_\mathrm{w} \cdot \mathbf{u}^{(1)} \quad \text{on} \quad \Gamma_\mathrm{w}, \tag{2.60}$$

$$\mathbf{u}^{(3)} = -\mathbf{K}^r \cdot \mathbf{u}^{(2)} \quad \text{on} \quad \Gamma_\mathrm{p}, \tag{2.61}$$

$$\mathbf{u}^{(4)} = -\mathbf{K}^r_\mathrm{w} \cdot \mathbf{u}^{(3)} \quad \text{on} \quad \Gamma_\mathrm{w}, \quad \text{etc..} \tag{2.62}$$

and in addition, for all n,

$$\mathbf{u}^{(n)} \to 0 \quad \text{as} \quad r \to \infty \tag{2.63}$$

The $\mathbf{K}^r$ and $\mathbf{K}^r_\mathrm{w}$ are the translational resistance tensor ratios for the particle and channel boundary (along width) respectively, and are present in the equations due to the violation of Galilean invariance in our system of consideration.

Each separate field is termed as reflexion from either Γ_p or Γ_w[17]. Among these, only the odd numbered fields contribute to the drag force, $\mathbf{F}$, exerted by the fluid on the particle. Therefore, the net force on the particle may be obtained by only summing these fields

$$\mathbf{F} = \mathbf{F}^{(1)} + \mathbf{F}^{(3)} + \mathbf{F}^{(5)} + ..., \tag{2.64}$$

where the initial field, $\mathbf{u}^{(1)}$, corresponds to the particle translating in an unbound fluid (note that in q2D unbound means that the bounding walls along width are at infinity, while the particle is still confined along height). Associated with this motion

$$\mathbf{F}^{(1)} = \mathbf{F}_\infty \tag{2.65}$$

In order to compute $\mathbf{u}^{(2)}$ we use the Lorentz reciprocal theorem for a particle suspended in an arbitrary flow field,

$$\iint\limits_{S_p} d\mathbf{S} \cdot \boldsymbol{\pi}^{(1)} \cdot \mathbf{u}^{(3)} = \iint\limits_{S_p} d\mathbf{S} \cdot \boldsymbol{\pi}^{(3)} \cdot \mathbf{u}^{(1)}, \tag{2.66}$$

where $\boldsymbol{\pi}^{(1)}$ and $\boldsymbol{\pi}^{(3)}$ denote the stress tensors associated with the corresponding velocity fields. By taking in the eqs. (2.59) and (2.65), we are led to the expression [18]

$$\mathbf{u}^{(3)} \cdot \mathbf{F}_\infty = \mathbf{U}_p \cdot \mathbf{F}^{(3)} \quad \text{on} \quad \Gamma_\mathrm{p} \tag{2.67}$$

Since $\mathbf{F}_\infty = -\mathbf{K}' \cdot \mathbf{U}_\mathrm{p}$, it follows from the above relation that

$$\mathbf{F}^{(3)} = -\mathbf{K}' \cdot \mathbf{u}^{(3)} \quad \text{on} \quad \Gamma_\mathrm{p} \tag{2.68}$$

Or, more precisely, for C being the hydrodynamic centre of the particle, using eq. (2.61)

$$\mathbf{F}^{(3)} = \mathbf{K}' \cdot \mathbf{K}^r \cdot \mathbf{u}_C^{(2)} = \mathbf{K}^0 \cdot \mathbf{u}_C^{(2)} \tag{2.69}$$

Using the knowledge of the mobility tensor we can write the boundary condition to be satisfied by $\mathbf{u}^{(2)}$ on Γ_w

$$\mathbf{u}^{(2)} = \mathbf{B}_\mathrm{p}(\mathbf{r}_\mathrm{w}) \cdot \mathbf{F}_\infty \quad \text{on} \quad \Gamma_\mathrm{w}, \tag{2.70}$$

where $\mathbf{B}_\mathrm{p}(\mathbf{r}_\mathrm{w})$ is the mobility tensor of the particle calculated for a point on Γ_w. From eq. (2.53) for any point on Γ_w, $\mathbf{B}_\mathrm{p}(\mathbf{r}_\mathrm{w})$ depends only on the relative distance, l, of the centre of particle to Γ_w, and is characterised by geometric shape of the wall. For c is the characteristic particle dimension, correct to $\mathcal{O}(c/l)$, $\mathbf{u}^{(2)}$ can sufficiently be expressed by the form

$$\mathbf{u}^{(2)} = \boldsymbol{\lambda}_\mathrm{w} \cdot \mathbf{F}_\infty \tag{2.71}$$

This dyadic variable $\boldsymbol{\lambda}_\mathrm{w}$ reduces to $\mathbf{B}_\mathrm{p}(\mathbf{r}_\mathrm{w})$ on Γ_w, and is independent of the shape of the particle, relying solely on the shape/nature of the bounding wall. Therefore, from eq. (2.69), we write

$$\mathbf{F}^{(3)} = \mathbf{K}^0 \cdot \boldsymbol{\lambda}_\mathrm{w} \cdot \mathbf{F}_\infty \tag{2.72}$$

It is noteworthy that $\boldsymbol{\lambda}_\mathrm{w}$ is an intrinsic function of l. By analogy to our previous calculation we can effectively replace $(\mathbf{u}^{(1)}, \mathbf{u}^{(2)})$ with $(\mathbf{u}^{(3)}, \mathbf{u}^{(4)})$ respectively, and redo the calculations. By doing so we obtain the higher-order reflections as

$$\mathbf{F}^{(2m+1)} = (\mathbf{K}^0 \cdot \boldsymbol{\lambda}_\mathrm{w})^m \cdot \mathbf{F}_\infty \quad \text{for} \quad m = 0, 1, 2, .. \tag{2.73}$$

After summing of the resulting geometric series and utilizing eq. (2.64), we obtain the force on the particle in presence of a finite wall as

$$\mathbf{F} = [\mathbf{I} - \mathbf{K}^0 \cdot \boldsymbol{\lambda}_\mathrm{w}]^{-1} \cdot \mathbf{F}_\infty = -[\mathbf{I} - \mathbf{K}^0 \cdot \boldsymbol{\lambda}_\mathrm{w}]^{-1} \cdot \mathbf{K}' \cdot \mathbf{U}_\mathrm{p} \tag{2.74}$$

Therefore, the translational resistance tensor of a particle moving in a finite medium is

$$\mathbf{K}'_{\text{finite}} = [\mathbf{K}^{-1} - \mathbf{K}^r \cdot \boldsymbol{\lambda}_\mathrm{w}]^{-1} \tag{2.75}$$

2.3.2.2 Rotation

For a particle rotating with angular velocity ω about its centre of hydrodynamic stress, its velocity at the surface is given by $\mathbf{u}_\mathrm{rot} = \mathbf{U} + \omega \times \mathbf{r}$. Thus for a point couple acting about the centre, $\mathbf{u}_\mathrm{rot}^{(1)} = \mathcal{O}(c/l)^m$, with $m > 2$ for a quasi-2D system. Thus when compared to translation, the relative rate of rotation is fairly small based on the range of (c/l) values considered, e.g. unless a particle is very close to the wall we can safely ignore the effect due to rotation in comparison to translation [18].

Chapter 3

Problem Formulation and Methods

3.1 Numerical Model

We study the transport of a rigid asymmetric particles in a micro-channel with rectangular cross section. The channel as discussed in section 2.2 has a characteristic dimension of height H and width W such that $H \ll W$. The shapes under consideration are built using discs as the elementary shape connected via rigid rectangular fibers. Thus we obtain more complex geometries upon assembling these basic shapes (fig. 1.1). The immersed particle having height, h_p, is strongly confined along the z direction and is transported by an imposed external flow with height-averaged flow velocity U_0. Thus, the particle essentially moves in two dimensions with its *transversal confinement*, $\beta = h_\mathrm{p}/H$, and the *lateral confinement* $\xi = c/W$.

At any point in time the particle's centre of mass is positioned at $(x(t), y(t))$ with respect to a reference point in the channel, and is oriented at angle $\theta(t)$ with respect to the stream direction. The distance between the top / bottom wall to the particle is defined by the gap size, $h_\mathrm{g} = (1-\beta)H/2$. A particle spanning the entire channel height has $\beta = 1$, whereas $\beta = 0$ corresponds to an infinitesimally thin body. The particle's translation and rotational velocities about centre of mass are represented using $\dot{x}_\mathrm{p}, \dot{y}_\mathrm{p}$ and $\dot{\theta}$.

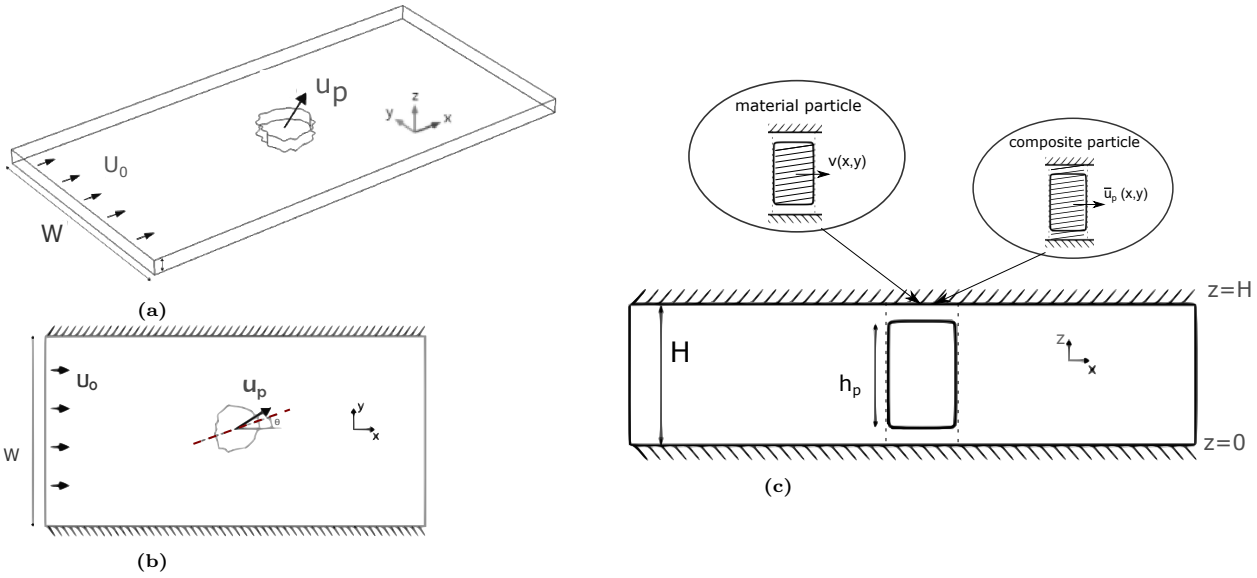

Figure 3.1: Projections of an arbitrary confined particle.(**a**) Q2D model of the channel with a particle of arbitrary shape suspended in it. The particle with height h_p along $\hat{z}$ is placed in a channel having a height H and width W, such that $H << W$. The stream with a mean flow velocity U_0 is directed along $\hat{i}$ (**b**) Top view of the channel in which the particle axis (red thick line) is oriented at an angle θ to the flow. The particle has an inplane motion with velocity $\mathbf{u}_\mathrm{p}$ (**c**) Side view of the channel showing the confinement and the dashed lines representing composite control volume in Q2D. The top and bottom of the wall is positioned at $z = 0$ and $z = H$ respectively.

In the system under consideration we use the depth-averaged Brinkman 2D equation to solve for the flow in fluid domain, $\Omega_\mathrm{f} = \Omega - \Omega_\mathrm{p}$, where Ω_p is the particle's in-plane cross-section. The fluid is in contact with boundaries represented by Γ_w and Γ_p for channel walls and particle respectively (see fig. 3.1b).

3.1.1 Composite Particle

When computing for the transport of rigid bodies within the proposed depth averaged approach, we primarily face two major challenges: (i) the modelling and evaluation of the gap flows and (ii) correlation of the material particle's velocity (fig. 3.1c) and stresses to those of the depth-averaged flow. To overcome these difficulties we introduce the concept of *composite control volume* - a 2D domain (Ω_p) composed of slices of fluid-particle-fluid fig. 3.1c. We propose to apply force and torque balance on this composite body as to be compatible with our depth-averaged approach. For a given gap size, $h_\mathrm{g} = bH$, e.g. $2b = 1 - \beta$, these slices spans from $[0, H]$ with the ranges $[0, bH]$ and $[(1-b)H, H]$ occupied by the liquid in the gaps and the range $[bH, (1-b)H]$ occupied by the rigid particle. The particle is assumed to be positioned at the centre of the channel (along height), such that the mid plane of the Hele-Shaw cell (at $z = H/2$) is also a plane of symmetry of the particle.

In the 2D representation of the composite particle, the effective velocity at any point in $(x, y) \in \Omega_\mathrm{p}$ for both the particle and liquid layers enclosed is denoted by $\bar{\mathbf{u}}_\mathrm{p}$. The velocity field for the rigid body's planar motion in the frame centred at *geometric centroid* of Ω_p can be written as,

$$\bar{\mathbf{u}}_\mathrm{p}(x, y) = \begin{pmatrix} 1 & 0 & -y \\ 0 & 1 & x \end{pmatrix} \cdot \begin{pmatrix} \dot{\bar{x}}_\mathrm{p} \\ \dot{\bar{y}}_\mathrm{p} \\ \dot{\bar{\theta}}_\mathrm{p} \end{pmatrix} \tag{3.1}$$

It is important to note that $(\dot{\bar{x}}_\mathrm{p}, \dot{\bar{y}}_\mathrm{p}, \dot{\bar{\theta}}_\mathrm{p})$ are not the velocities of the material point in the particle in q2D (x, y, z), but rather the depth-averaged velocity of the composite body.

3.1.2 Stress on the composite particle

The depth-averaged stress tensor due to the force exerted by the fluid on the composite particle's lateral walls (Γ_p) can be denoted by, $\boldsymbol{\pi}_\mathrm{2D} = -\mathrm{I}p + \mu(\boldsymbol{\nabla}\mathbf{u} + \boldsymbol{\nabla}\mathbf{u}^\dagger)$. Thus, the H averaged force, $\bar{\mathbf{f}}$, acting per unit length along z, is used to compute the total force acting on the composite particle:

$$\bar{\mathbf{F}}_\mathrm{2D} = H\,\bar{\mathbf{f}} \tag{3.2}$$

However, we are not interested in knowing the forces on the composite particle. Instead, more specifically, we like to calculate the forces acting on the material points of the particle's surface. For this we take the aid of an ansartz velocity profile, $q(z)$, introduced in [19]. Although it has been used to define the velocity profile in the domain Ω_p for rectangular fibres, at this point we extend it to any complex geometry by making an educated guess to apply it only close to the fluid interface at Γ_p. It defines the full 3D velocity of the fluid, $\mathbf{v}(x, y, z) = \mathbf{u}(x, y)\, q(z)$, in q2D adjacent to the particle sides, and requires that its mean value over the channel height (H) equals 1, e.g. $(1/H)\int_0^H q(z)\, dz = 1$, such that

$$q(z) = \frac{6}{(1-\beta^3)}\left[\left(1 - \frac{z}{H}\right)\frac{z}{H}(\mathbb{1}_{[0,bH]} + \mathbb{1}_{[(1-b)H,H]}) + (1-b)b\mathbb{1}_{[bH,(1-b)H]}\right], \tag{3.3}$$

where $\mathbb{1}_{[a,b]}$ is the indicator function which takes the value of 1 when z is within the range $[a, b]$ and 0 elsewhere. the profile of the ansartz obtained using different confinement ratios is shown in fig. 3.2

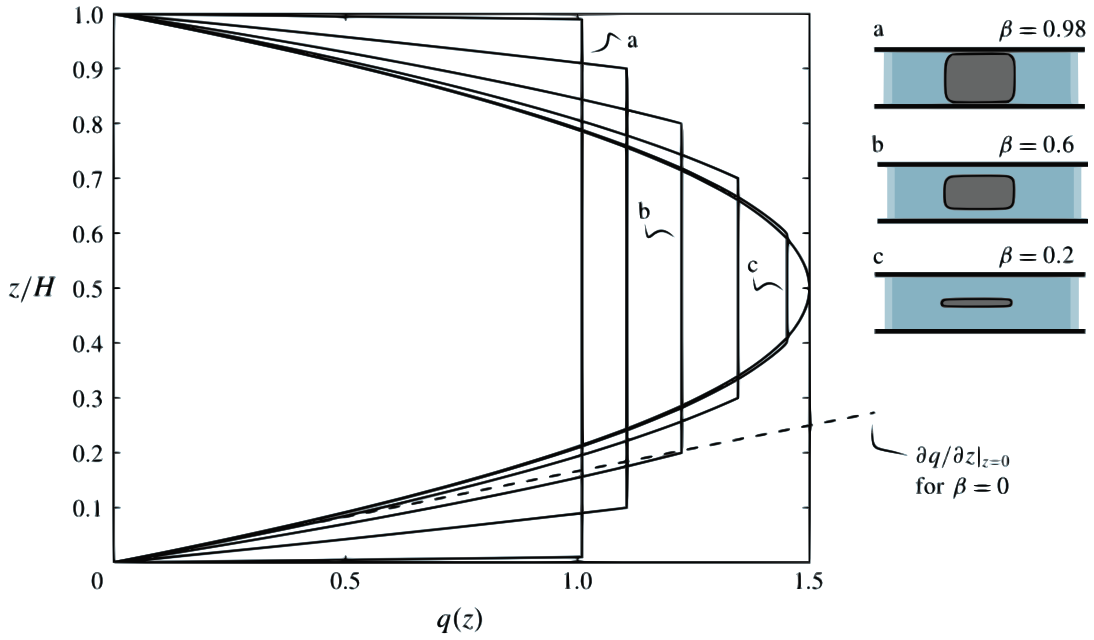

Figure 3.2: Model velocity profiles for fluid close to the lateral sides of the particle. The flat regions represent where the material particle is located and has a constant velocity equal to that of the rigid body. The tangent (dashed line) illustrates the velocity gradient for $\beta = 0$. (image as taken from [19])

Thus in principle only on the flat regions (marked using $a/b/c$ in fig. 3.2) where the material body is located the fluid imparts viscous and pressure forces on particle sides. Hence, it is necessary to consider only this region of the fluid velocity to compute the viscous stress exerted on the particle. Further, using the ansartz we can estimate the magnitude of the fluid's velocity field in this region as

$$\mathbf{v}(x,y) = \mathbf{u}(x,y)\frac{6}{(1-\beta^3)}(1-b)b \qquad \text{for} \qquad (x,y) \in \Gamma_{\mathrm{p}} \ \cup \ z \in [bH, (1-b)H] \tag{3.4}$$

Upon substituting the value of b in the above equation, we get

$$\mathbf{v}(x,y) = \mathbf{u}(x,y)\frac{3}{2}\frac{1+\beta}{1+\beta+\beta^2} = \mathbf{u}(x,y)\ \varphi(\beta) \qquad \text{for} \qquad (x,y) \in \Gamma_{\mathrm{p}} \ \cup \ z \in [bH, (1-b)H] \tag{3.5}$$

The viscous stress, $\boldsymbol{\pi}_{vc}$, on the lateral side of the particle can be estimated using the velocity gradient over Γ_{p}

$$\boldsymbol{\pi}_{vc} = \mu\left(\frac{\mathbf{u}_{\mathrm{p}} - \mathbf{v}(x,y)}{\Delta n}\right) = \mu\left(\frac{\mathbf{u}_{\mathrm{p}} - \varphi(\beta)\ \mathbf{u}}{\Delta n}\right), \tag{3.6}$$

where Δn is the difference in position along $\hat{n}$, for $\hat{n}$ is the direction normal to an element of Γ_{p} pointing towards fluid. But instead, from the 2D model we evaluate the stress as

$$\{\boldsymbol{\pi}_{vc}\}_{2\mathrm{D}} = \mu\left(\frac{\bar{\mathbf{u}}_p - \mathbf{u}}{\Delta n}\right) \tag{3.7}$$

In the above equation, by taking the value of $|\Delta n|$ equals 1 we can estimate an equivalent-effective fluid velocity $\mathbf{u}$ regularly spaced at 1 normal distance from each differential element of Γ_{p}. This equivalent velocity will imitate the difference in velocities $(\bar{\mathbf{u}}_p - \mathbf{u})$ around the particle boundaries for a discretized distance of length 1 (Δn) along $\hat{n}$ for each boundary element. Thus by substituting this effective velocity from eq. (3.7) into eq. (3.6), we can compute the viscous stress acting on the sides of the material particle as

$$\boldsymbol{\pi}_{vc}/\mu = \mathbf{u}_{\mathrm{p}} - \varphi(\beta)\,(\bar{\mathbf{u}}_{\mathrm{p}} - \{\boldsymbol{\pi}_{vc}\}_{2\mathrm{D}}/\mu) \tag{3.8}$$

For pressure, however, we still assume $\partial_z p = 0$ on particle sides and use the pressure stress, $\{\boldsymbol{\pi}_{ps}\}_{\text{2D}}$, obtained from 2D simulation for force estimation. Thus in our present numerical model,

$$\boldsymbol{\pi}_{ps} = \{\boldsymbol{\pi}_{ps}\}_{\text{2D}} \qquad \text{for} \qquad (x, y) \in \Gamma_{\text{p}} \ \cup \ z \in [bH, (1-b)H] \tag{3.9}$$

The net force acting on lateral side of the particle, $\mathbf{F}_l$, is

$$\mathbf{F}_l = h_{\text{p}} \int_{\Gamma_{\text{p}}} (\boldsymbol{\pi}_{vc} + \boldsymbol{\pi}_{ps}) \cdot d\boldsymbol{\Gamma}_{\text{p}}, \tag{3.10}$$

where, $d\boldsymbol{\Gamma}_{\text{p}} = \|d\boldsymbol{\Gamma}_{\text{p}}\| \, \hat{n}$. In order to calculate the total force acting over the material particle's surface (summation of forces on the sides and in gaps), it is necessary to have an idea on the flow pattern in the gaps.

3.1.3 Gap-flow Model

Since the Brinkman-2D formalism for q2D flows does not include the model for flows in the gap region, we plug in an additional distinct equation as to determine the shear at the top and bottom walls of the material particle. Here along z we have the stationary walls of the channel, with the other ends of the gaps a moving boundary of the particle as shown in fig. 3.3.

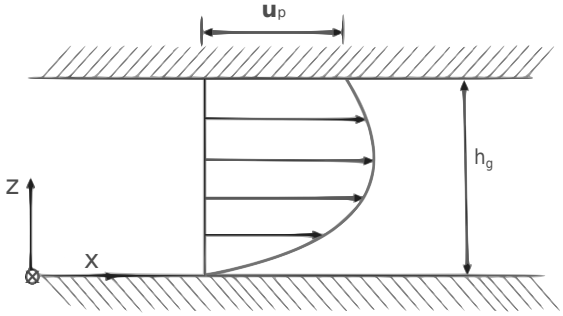

Figure 3.3: Hybrid Couette flow in gaps. Image represents the Couette flow within gap at the bottom of the material particle. The particle surface is moving with a velocity $\mathbf{u}_p$ at a distance h_{g} from the stationary wall. (source[20])

For this condition we use the simple decoupled governing equation for flow between two-parallel plates

$$\partial_x p = \mu \, \partial_z^2 (\mathbf{v} \cdot \hat{i}) \quad \text{and} \quad \partial_y p = \mu \, \partial_z^2 (\mathbf{v} \cdot \hat{j}) \tag{3.11}$$

with the boundary values: (a) at $z = 0$, $\mathbf{v} = 0$ (b) at $z = h_{\text{g}}$, $\mathbf{v} = \mathbf{u}_{\text{p}}$ for the bottom of the particle. Upon invoking these boundary conditions for the solution of the above equation, we end up with[20]

$$\mathbf{v} = \frac{z}{h_{\text{g}}} \mathbf{u}_{\text{p}} - \frac{h_{\text{g}}^2}{2\mu} \frac{z}{h_{\text{g}}} \left(1 - \frac{z}{h_{\text{g}}}\right) \boldsymbol{\nabla} p, \tag{3.12}$$

where, $\mathbf{u}_{\text{p}} = \mathbf{U}_{\text{p}} + \omega \times \mathbf{r} \quad \text{on} \quad \Omega_{\text{p}}$.

Thus for very high confinements ($\beta \sim 1$) a linear velocity profile (simple Couette flow) is imposed. While for slightly low ranges ($\beta \sim 0.8$) the Poiseuille profile takes effect in spirit of a hybrid flow. The velocity profile of the Couette flow from positive to negative pressure gradients is represented in the figure below (fig. 3.4)

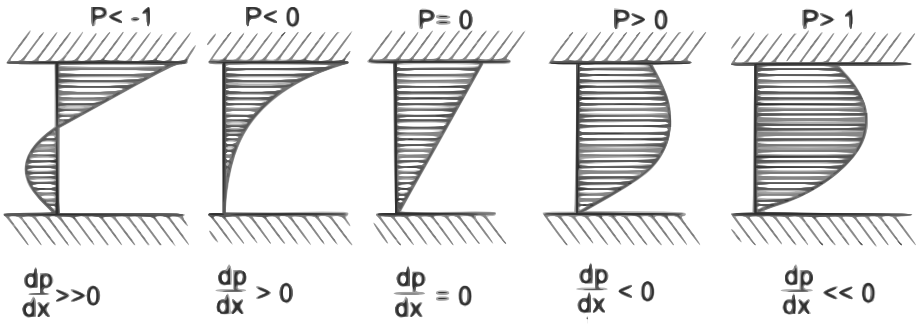

Figure 3.4: Effect of pressure on Couette flow in gaps. Flow with a moving top surface and pressure gradient along x. Starting from left we impose positive pressure gradient to negative pressure gradient on the right. (source [20])

The force on the particle in the gaps (transversal sides of the particle), $\mathbf{F}_t$, is given by the velocity gradient over the particle surface at $z \in \{h_\mathrm{g},\ H - h_\mathrm{g}\}$

$$\mathbf{F}_t = 2\,\mu \iint_{\Omega_\mathrm{p}} [\partial_z \mathbf{v}]_{z=h_\mathrm{p}}\, d\Omega_\mathrm{p}, \tag{3.13}$$

where $d\Omega_\mathrm{p}$ is an elemental *scalar surface area* of the domain Ω_p, and the factor 2 takes into account that we have gaps both in the top and bottom of the particle. Upon solving for the partial derivative and applying the limit, $z = h_\mathrm{g}$, we obtain

$$\mathbf{F}_t = 2\,\mu \iint_{\Omega_\mathrm{p}} \left(\frac{\mathbf{u}_\mathrm{p}}{h_\mathrm{g}} + \frac{h_\mathrm{g}}{2\mu} \boldsymbol{\nabla} p \right)\, d\Omega_\mathrm{p} \tag{3.14}$$

3.1.4 Numerical simulation

In this work, for the numerical resolution of the linear differential equation - Brinkman 2D, we propose Finite Element Method (FEM) as the suitable technique. We employ COMSOL Multiphysics[§] for solving the depth-averaged flow equation as to estimate the fields $\mathbf{u}$ and p, for which, the creeping flow physics package with shallow channel approximation is chosen. Using these solutions, we determine the forces acting on the material particle and estimate its trajectories of motion with the numerical scheme detailed below.

At a given initial position of the particle $(x_\mathrm{p}, y_\mathrm{p})$ and orientation θ, both the resistance tensors - $\mathbb{R}^0$ and $\mathbb{R}'$ (which are functions only of the system geometry) can be calculated by using appropriate boundary conditions. Note that *system geometry* includes both particle and channel boundaries.

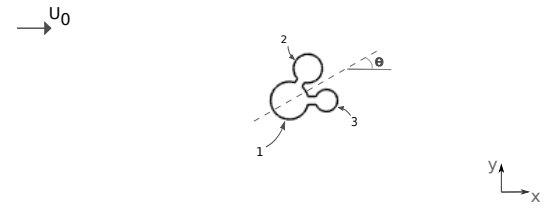

Figure 3.5: Configuration of a shape under consideration in a Brinkman flow. Image shows a tripod consisting of three discs, assembled via two rectangular connectors of width 13.6875 μm each. The discs are denoted by 1, 2 and 3 respectively in the clock-wise direction, with their centres 1-2 and 1-3 positioned at 62.5 μm from each other. The angular bisector between these connectors is oriented at an angle θ to the flow. The diameter of disc 3, d_3, is chosen to be 37.5 μm, with the size of other discs defined using ratios λ and κ: for $\lambda = d2/d3$ and $\kappa = d1/d3$.

[§]COMSOL Livelink for MATLAB is used to manipulate the data variables in the model created using COMSOL. In addition, using MATLAB, we can reproduce the features (e.g. gap flow) which are absent in the 2D COMSOL model.

3.1.4.1 Estimation of $\mathbb{R}^0$

As previously discussed, from section 2.2.4 we can write

$$\begin{pmatrix}\mathbf{F}^0\\ \mathbf{T}^0\end{pmatrix} = \mu\mathbb{R}^0 \cdot \mathbf{U}_0 \quad \Longrightarrow \quad \mathbb{R}^0 = (1/\mu)\begin{pmatrix}\mathbf{F}^0\\ \mathbf{T}^0\end{pmatrix} \cdot \mathbf{U}_0^{-1} \tag{3.15}$$

For a given particle geometry, e.g. fig. 3.5, the forces ($\mathbf{F}_l^0$), and hence the torque ($\mathbf{T}_l^0$) on the particle sides (Γ_p) can be computed using eq. (3.10). Since $\mathbb{R}^0$ is an intrinsic property of the system configuration we can choose to have any velocity for the streaming fluid ($\mathbf{U}_0$). The boundary conditions for this solution would be: (a) $\mathbf{U}_0 = 1\,\hat{i}$ for the stream velocity at the inlet of the channel far away from the particle, and (b) $\bar{\mathbf{u}}_\mathrm{p} = 0$. This strong hypothesis for the composite particle velocity is reasonable since the hydraulic resistance in the thin gaps is larger than that around the particle. From [21], it is estimated to be $\mathcal{O}(b^{-3})$ larger than the lateral portion.

Further, using eq. (3.14) it is possible to estimate forces and torques ($\mathbf{F}_t^0, \mathbf{T}_t^0$) on the top and bottom of the particle provided the pressure (p) is estimated on Γ_p. Thus, for forces in the gaps along $\hat{i}$, we need to evaluate the pressure difference between the x-coordinate ends of each

$$y = \Xi(x), \quad x \in \Gamma_\mathrm{p}, \tag{3.16}$$

where Ξ is the parametric curve function of Ω_p. The generation of these sets of discrete points is done using MATLAB. A polygon of the given shape with its initial orientation is created using the Polyshape tool (available from MATLAB R2017b); over which a shape similar to grill coil is drawn, see fig. 3.6a.

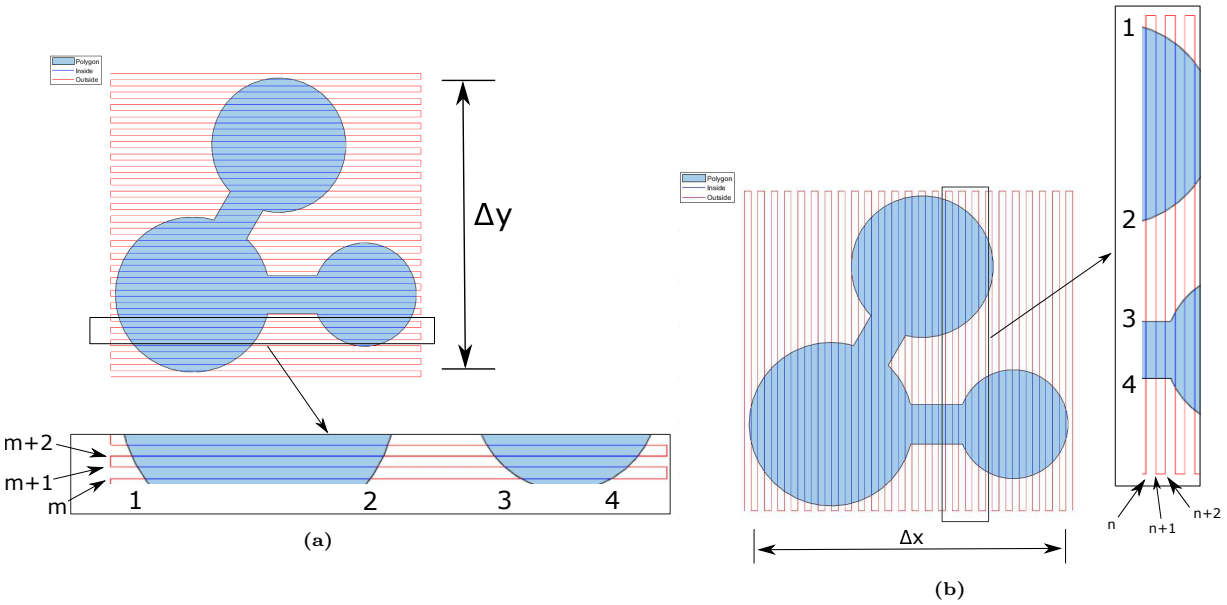

Figure 3.6: Estimation of the horizontal and vertical intercepts for pressure evaluation. (**a**) Horizontally oriented grill coils for the estimation of $\partial_x p$ across the particle (**b**) Vertically oriented grill coils for the estimation of $\partial_y p$ across the particle. In both cases above the number of intercepts along a line is marked with numbers. The Δy and Δx represent the extreme difference in the corresponding coordinates on Γ_p for when the particle is oriented at any angle. Also the naming has been done using m, n for the horizontal and vertical strips respectively.

The coils always remain parallel to the flow (irrespective of particle orientation at any time t), and the intercepts of the coils and Γ_p are then supplied to COMSOL for pressure evaluation. Each set of data points, e.g. (x_1, y_1) & (x_2, y_1) on the same row of the coil is chosen for pressure gradient ($\partial_x p$) calculation. As known, in some cases a row of the grill might have more than two intercepts : e.g. $2q$ (in fig. 3.6a). In such instances the intercepts are always even and can be grouped into q sets starting from any extreme end. Furthermore, the particle is divided into thin strips with the coil rows as its respective centreline, meaning the total number of strips is equal to the number of data sets. Thus summing up the areas of these horizontal

strips would give the total area of the domain $\Omega_{\rm p}$. The total force acting along $\hat{i}$ on an m^{th} strip can be computed as,

$$\{F_t\}_{x,m} = \mu \left(\frac{\mathbf{u}_{\rm p}}{h_{\rm g}} + \frac{h_{\rm g}}{2\mu}\boldsymbol{\nabla} p\right)_m \cdot \frac{(x_{1,m} - x_{2,m})\{\Delta y\}_{\Gamma_{\rm p}}}{(M+1)}\,\hat{i}, \tag{3.17}$$

where $\{\Delta y\}_{\Gamma_{\rm p}}$ is the extreme y-coordinate difference on $\Gamma_{\rm p}$ and M is total count of the number of grill rows making an effective intercept with the polygon. $(x_{1,m} - x_{2,m})$ is the difference of the horizontal ends on a strip, with $\partial_x p$ calculated using the positions of the latter. The corresponding torque due to the x-component of the force, $\{\mathbf{T}_t\}_{x,m}$, on the same strip located at the vertical position, $y = y_m$, from the point of interest is

$$\{\mathbf{T}_t\}_{x,m} = (y_m\,\hat{j}) \times \{\mathbf{F}_t\}_{x,m} \tag{3.18}$$

Thereon, due to the flow in the gaps as a result of pressure difference, the total force and torque (due to the x-component of the force) acting in the gaps of a stationary material particle is calculated to be

$$\{\mathbf{F}_t^0\}_x = 2\sum_{m=1}^{M+1}\{\mathbf{F}_t^0\}_{x,m} \quad \text{and} \quad \{\mathbf{T}_t^0\}_x = 2\sum_{m=1}^{M+1}\{\mathbf{T}_t^0\}_{x,m} \tag{3.19a, 3.19b}$$

In a similar manner, for the y-component of the gap force on the particle, we make use of strips always perpendicular to the flow as to determine the datasets and its corresponding pressure gradient $(\partial_y p)$/areas, refer to fig. 3.6b. The total force acting along $\hat{j}$ on an n^{th} strip can be computed as,

$$\{F_t\}_{y,n} = \mu \left(\frac{\mathbf{u}_{\rm p}}{h_{\rm g}} + \frac{h_{\rm g}}{2\mu}\boldsymbol{\nabla} p\right)_n \cdot \frac{(y_{1,n} - y_{2,n})\{\Delta x\}_{\Gamma_{\rm p}}}{(N+1)}\,\hat{j}, \tag{3.20}$$

where $\{\Delta x\}_{\Gamma_{\rm p}}$ is the extreme x-coordinate difference on Γ_p, and $(y_{1,n} - y_{2,n})$ is the difference of the vertical ends on a strip; with $\partial_y p$ calculated using the positions of the latter. N is the total number of grill columns making an effective intercept with the polygon. In addition, the fineness of the grill (distance between successive rows/colmns) can be changed as to increase the accuracy of the result.

Therefore, the total force and torque in the gap is

$$\mathbf{F}_t^0 = \{\mathbf{F}_t^0\}_x + \{\mathbf{F}_t^0\}_y \quad \text{and} \quad \{\mathbf{T}^0\}_t = \{\mathbf{T}_t^0\}_x + \{\mathbf{T}_t^0\}_y \tag{3.21a, 3.21b}$$

which leads to the estimation of $\mathbf{F}^0$ and $\mathbf{T}^0$

$$\begin{pmatrix}\mathbf{F}^0\\ \mathbf{T}^0\end{pmatrix} = \begin{pmatrix}\mathbf{F}_l^0\\ \mathbf{T}_l^0\end{pmatrix} + \begin{pmatrix}\mathbf{F}_t^0\\ \mathbf{T}_t^0\end{pmatrix}, \tag{3.22}$$

and subsequently the $\mathbb{R}^0$.

3.1.4.2 Estimation of $\mathbb{R}'$

Again, from section 2.2.4 we can write

$$\begin{pmatrix}\mathbf{F}'\\ \mathbf{T}'\end{pmatrix} = -\mu\mathbb{R}'\begin{pmatrix}\mathbf{U}_{\rm p}\\ \omega_{\rm p}\end{pmatrix} \quad \Longrightarrow \quad \mathbb{R}' = -(1/\mu)\begin{pmatrix}\mathbf{F}'\\ \mathbf{T}'\end{pmatrix}\begin{pmatrix}\mathbf{U}_{\rm p}\\ \omega_{\rm p}\end{pmatrix}^{-1} \tag{3.23}$$

The boundary value for this problem would be: (a) $\mathbf{U}_0 = 0$ for the stream velocity at the inlet of the channel far away from the particle, and (b) $\mathbf{U}_{\rm p} = \dot{x}_{\rm p}\,\hat{i} + \dot{y}_{\rm p}\,\hat{j}$, $\omega_{\rm p} = \dot{\theta}_{\rm p}\,\hat{k}$ for the material particle. $\mathbb{R}'$ being an intrinsic value of the system geometry, we prescribe a sets of particle velocities: $(\dot{x}_{\rm p}, \dot{y}_{\rm p}, \dot{\theta}_{\rm p}) \equiv \{(1,0,0),(0,1,0),(0,0,1)\}$, one after the other, and calculate its corresponding forces and torque. The force and torue calculated using each set will correspond to the individual columns of $\mathbb{R}'$. For example, when a particle is given a unit velocity along x, the resultant force and torque (a 3×1 matrix) is equal to the values of the first column of the resistance tensor $\mathbb{R}'$. For 2D, however, we need to provide composite particle velocities. To do this, for a confined particle in motion in otherwise quiescent fluid, we can take a simple couette flow in the gaps (see fig. 3.7).

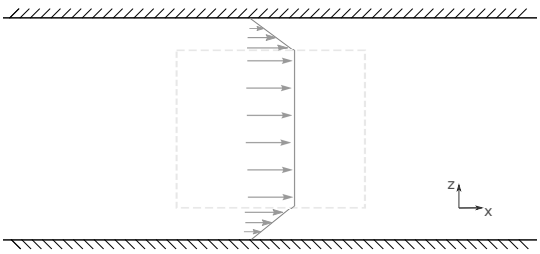

Figure 3.7: Simple Couette flow in the gaps. Figure shows the z velocity profile for a composite particle moving in an otherwise quiscent fluid

Here by taking the average of the velocity profile in range of $z \in [0, H]$ we can compute the composite particle velocity as

$$\begin{aligned}\bar{\mathbf{u}}_{\mathrm{p}} &= (2/H)\int_0^{H/2}\left[\left(\frac{\mathbf{u}_{\mathrm{p}}}{h_{\mathrm{g}}}\right)\mathbb{1}_{[0,bH]} + \mathbf{u}_{\mathrm{p}}\mathbb{1}_{[bH,H/2]}\right]dz \\ &= \mathbf{u}_{\mathrm{p}}(\beta + bH)\end{aligned} \tag{3.24}$$

In the above equation we are calculating the average only for the bottom half of the channel since it is symmetric about plane $z = H/2$. Imposing this velocity ensures the mass balance around the particle in Brinkman 2D. Therefore, we can estimate the total forces ($\mathbf{F}'$) and torque ($\mathbf{T}'$) acting on the material particle using eqs. (3.10), (3.17) and (3.20); considering that the pressure buildup across the particle due to its motion contributes to $\partial_x p$ and $\partial_y p$ in the gap force equation, even though we take simple Couette flow for mass balance. This assumption is valid because the hydraulic resistance in the gaps is several orders of magnitude higher compared to the lateral portion.

3.1.4.3 Force and Torque Free Velocity

Using the knowledge of $\mathbb{R}^0$ and $\mathbb{R}'$ for current configuration we can calculate the *force and torque free velocity* of the particle using eq. (2.34)

$$\begin{pmatrix}\mathbf{U}_{\mathrm{p}} \\ \omega_{\mathrm{p}}\end{pmatrix} = \mathbb{R}'^{-1}\cdot\mathbb{R}^0\cdot\mathbf{U}_0 = \mathbb{R}^r\cdot\mathbf{U}_0 \tag{3.25}$$

For our cases, in the absence of particle within the channel, the flow is directed along $\hat{i}$ ($\mathbf{U}_0\cdot\hat{j} = 0$). Accordingly, we try to non-dimensionalize the velocities and lengths with respect to U_0 and H respectively. Thus

$$\begin{pmatrix}\mathbf{U}^*_{\mathrm{p}} \\ \omega^*_{\mathrm{p}}\end{pmatrix} = \mathbb{R}^r\cdot\begin{pmatrix}1\\0\end{pmatrix}, \tag{3.26}$$

where $(\mathbf{U}^*_{\mathrm{p}}, \omega^*_{\mathrm{p}})$ are the dimensionless velocities, and

$$\mathbf{U}^*_{\mathrm{p}} = \mathbf{U}_{\mathrm{p}}/U_0, \quad \omega^*_{\mathrm{p}} = \omega_{\mathrm{p}}(H/U_0) \tag{3.27}$$

We compute the resistance tensors about the *geometric centroid* of the particle, since we can kinematically differentiate between absolute translation and rotation about this point. Subsequently, we can establish a first order kinematic equation as follows

$$x^*_{\mathrm{p}}(t^* + \Delta t^*) = x^*_{\mathrm{p}}(t) + \dot{x}^*_{\mathrm{p}}\,\Delta t^* \tag{3.28}$$

$$y^*_{\mathrm{p}}(t^* + \Delta t^*) = y^*_{\mathrm{p}}(t) + \dot{y}^*_{\mathrm{p}}\,\Delta t^* \tag{3.29}$$

$$\theta^*(t^* + \Delta t^*) = \theta^*(t) + \dot{\theta}^*\,\Delta t^* \tag{3.30}$$

The above numerical time integration scheme is performed with the calculated values at a dimensionless time, $t^* = t(U_0/H)$, as to estimate the position and orientation of the particle at the next time step, Δt^*.

The appropriate value for Δt^* is chosen such that, $\Delta t^* < H^2/\nu$, where ν is the kinematic viscosity of the fluid. This new configuration at $t^* + \Delta t^*$ is evaluated again for the new $\mathbb{R}^r$ and its respective force and torque free velocities. By repeating this cycle over and over again we can obtain the trajectory and angular orientations of the particle over a period of time, fig. 3.8.

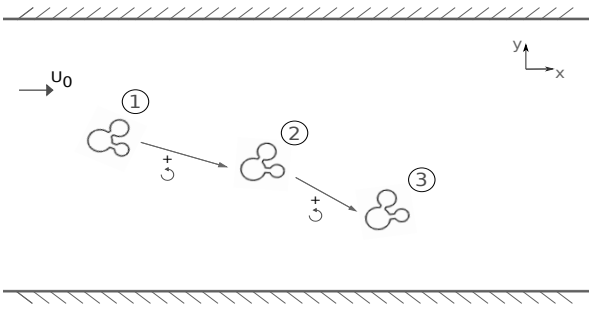

Figure 3.8: The trajectory of a simultaneously rotation and translating body. The markings 1,2,3 represents the system configuration at time t^*, $t^* + \Delta t^*$ and $t^* + 2\Delta t^*$ respectively. At each time point we evaluate the instantaneous force and torque free velocities of the particle using quasi-steady approximation, and estimate its next position and orientation by applying first order time integration scheme.

3.2 Experimental Technique

Free-radical photo polymerization is an effective technique for the synthesis of polymeric particles at the micron scale. Light-sensitive photoinitiator molecules present within an oligomer generate highly reactive free radicals upon reacting with photons of light. These radicals upon attacking the reactive double bond groups on monomer/oligomer molecules initiate the polymerization process. A well-defined shape using photomasks can be rapidly polymerised through cross-linking reaction of multifunctional molecules containing multiple reactive groups. Thus large numbers of particles with complex shapes (mask-defined geometry) can be produced through *stop-flow lithography* (SFL) in a stationery film of oligomer - typically containing acrylate groups.

Among the possible chain terminating steps, the ability of oxygen to react with these radical species to form peroxide molecules is dominant at places having high oxygen concentration. When polymerizing over a surface of PDMS, the permeability of PDMS to oxygen can be exploited to ensure that there is an un-cross-linked layer of liquid inbetween the formed polymer network and the wall. The inhibition of the free radicals at the surface within a micro channel such as ours, can be utilized to produce "free-standing particles" having lubricating layers symmetrically at both the top and bottom walls of the PDMS device (fig. 3.9).

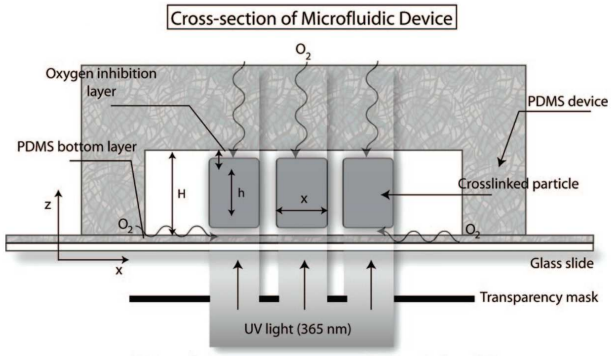

Figure 3.9: Stop-flow Lithography. Cross-sectional view of cuboidal particles formed by projecting UV light over a film of oligomer enclosed in an all-PDMS device. (image as taken from [22])

A simplified set of reaction mechanisms used to describe the free radical polymerization is displayed in

table 3.1. Here the photo-cleaved initiator molecules form the primary radical species ($\dot{\mathrm{R}}$), which then reacts with an oligomer molecule (M) to initiate the chain. This newly generated radical species ($\mathrm{R}\dot{\mathrm{M}}$) further consume the available oligomer with unconverted double bonds to form larger radical, given by the rate constant k_p. Thus the number of radicals is unaffected in above mentioned step. The depletion of the radicals occurs either when they react with each other: with rate constant k_t, or when they form peroxides with oxygen: with rate constant k_O.

Table 3.1: Simplified reaction mechanism for free radical polymerization. (as taken from [22])

no.	reaction	mechanism step
1	$\mathrm{PI} \xrightarrow{h\nu} \dot{\mathrm{R}}$	photolysis
2	$\dot{\mathrm{R}} + \mathrm{M} \rightarrow \mathrm{R}\dot{\mathrm{M}}$	chain inititation
3	$\mathrm{R}\dot{\mathrm{M}}_n + \mathrm{M} \xrightarrow{k_p} \mathrm{R}\dot{\mathrm{M}}_{n+1}$	chain propagation
4	$\mathrm{R}\dot{\mathrm{M}}_n + \mathrm{R}\dot{\mathrm{M}}_m \xrightarrow{k_t} \mathrm{RM}_n\mathrm{M}_m$	chain termination
5	$\mathrm{R}\dot{\mathrm{M}}_n + \mathrm{O}_2 \xrightarrow{k_o} \mathrm{RM}_n\mathrm{OO}$	inhibition

A quasi-steady approximation equating the rate of radical production and consumption is used for the reaction scheme specified above. As soon as the oxygen dissolved in the oligomer film drops below a critical value, it signals the onset of gelation. Due to the mass transport of oxygen from all-PDMS channel walls the polymerization front proceeds from the channel center. This occurs after an induction time τ_i is reached. The absence of oxygen almost instantaneously favours oligomer conversion until a critical particle height is achieved. The critical oligomer conversion fraction of 0.98 is enough to calculate the dimensionless gap height, $\delta_{i,c}$, and hence the height of the particle.

As the particles are usually formed far away from the side walls, the layer of oxygen inhibition is considered only at the top and bottom walls of the device. Thus, cross-linked particles grow symmetrically outward about the channel center, comprising of the un-cross-linked oligomer on either side of the cross-linked polymer. The higher diffusivity of oxygen in PDMS when compared to PEGDA imposes equilibrium, $[O_{2,\mathrm{eq}}]$, - free diffusion on channel walls. The dimensionless parameters, (Da_1, Da_2, α), in this model are used to reveal the dependence of τ_i and $\delta_{i,c}$ on light intensity (I_0) and photo-initiator concentration ([PI]).

$$Da_1 = \frac{k_O^2 H^2 [O_{2,\mathrm{eq}}]}{2 k_t D_O}, \qquad Da_2 = \frac{k_p k_O H^2 [O_{2,\mathrm{eq}}]}{2 k_t D_O}, \qquad \alpha = \frac{4\varphi\epsilon[\mathrm{PI}] I_0 k_t}{k_O^2 [O_{2,\mathrm{eq}}]^2} \tag{3.31}$$

where, φ is the quantum yield of formation of initiating radicals and ϵ the molar extinction coefficient of the photoinitiator. Da_1 and Da_2, respectively are the ratio of the rate of oxygen inhibition to its diffusion into the oligomer and the ratio of rate of radical propagation to the diffusion of oxygen into the oligomer. Further Da_1 and α can be lumped to form the Damköhler number, $Da = Da_1\alpha/2$.

Thus for large Da we would have an increased rate of radical formation / oxygen consumption (the rate of oxygen depletion is zero-order in the oxygen concentration), thereby depleting way more oxygen than that can be diffused into. Also a small Da_2 would mean a decreased amount of free radicals participating in chain propagation soon after τ_i; thus tapering out the increase in particle height beyond $\delta_{i,c}$. For the above two conditions, the analytical solution resulting from the rate expressions and species balance can be explained using simple scaling relations,

$$\tau_i = \frac{\pi}{4Da} \qquad \delta_{i,c} \simeq \delta_p \sim \frac{1}{Da^{1/2}} \tag{3.32}$$

in which δ_p is defined as the penetration depth of oxygen inside the oligomer. In addition, as seen form the above mentioned scaling laws, Da_2 is found to have little influence on both.

In the prior model of consideration, the following are the assumptions made:

- high surface area to volume ratio of the micro-fluidic devices ensures zero thermal gradient within system.
- all the dimensionless numbers in the model are invariant with oligomer conversion
- there are no trapping of radical species - every radical species formed participates in the reaction mechanisms mentioned.
- the diffusion of oligomeric species is neglected in the mass transport equation as the molecule size is large compared to oxygen.
- the intensity does not attenuate over the channel depth due to the absorption by PI - the molar extinction coefficient, ϵ, characterizes the absorption at 362 nm.
- constant oligomer viscosity

3.2.1 Materials and Preparation

3.2.1.1 Microfluidic Device

Microchannels are fabricated by pouring polydimethylsiloxane (PDMS, Sylgard 184, Dow Corning) over a silicon wafer containing positive-relief features. The PDMS and the silicone elastomer are mixed in 7:1 ratio by mass, centrifuged at 7400 rpm for 15 minutes, and allowed to cure over night inside an oven maintained at $65°C$. Before placing it in the oven, it is also recommended to place the PDMS mixture + mould inside a vacuum chamber at 100 mbar for 30 minutes to get rid of the air bubbles. Channels with a rectangular cross section of height 33 μm and width 512 μm, with a typical length of 2.4 cm were used.

Each individual channel is cut out using a scalpel and then punched holes at the ends to make inlets and outlets. The channels are then laminated using glass slides spin-coated with PDMS (containing 10:1 ratio, centrifuged and cured for 35 minutes at $65°C$) as to ensure uniformity in the channel boundary. Finally, the device is placed in the oven overnight for use.

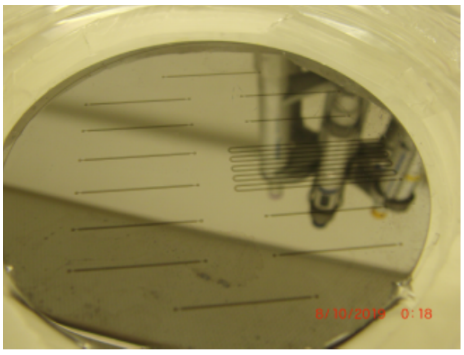

(a)

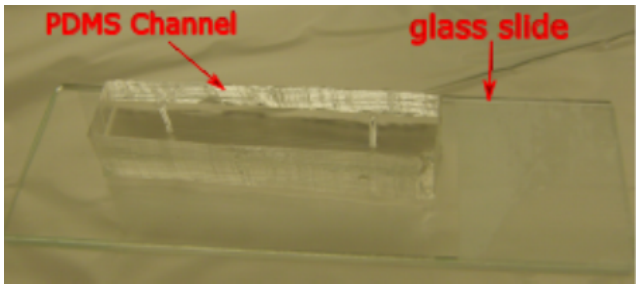

(b)

Figure 3.10: Preparation of the microfluidic device. (**a**) A microfluidic channel mould with positive features for channel preparation. (**b**) A microfluidic device: channels laminated over a PDMS coated glass slide.

3.2.1.2 Photoreactive Solution

The pre-polymer solution is prepared using poly(ethylene glycol) (250) diacrylate (PEG-DA, Sigma Aldrich) and a photoinitiator with 90% and 10 % by volume respectively. 2-hydroxy-2- methyl-1-phenyl-1-propanone (Darocur 1173, Sigma Aldrich) is used as photoinitiator due to its low aborbance. The Eppendorf tube containing the solution is covered with Aluminium foil to avoid photo-polymerization. The solution is then well mixed using a vortex mixer and then is centrifuged at 6000 rpm for 10 minutes. By using a 1 ml syringe the mixture is loaded to a precision tip, which thereafter is inserted into the device inlet.

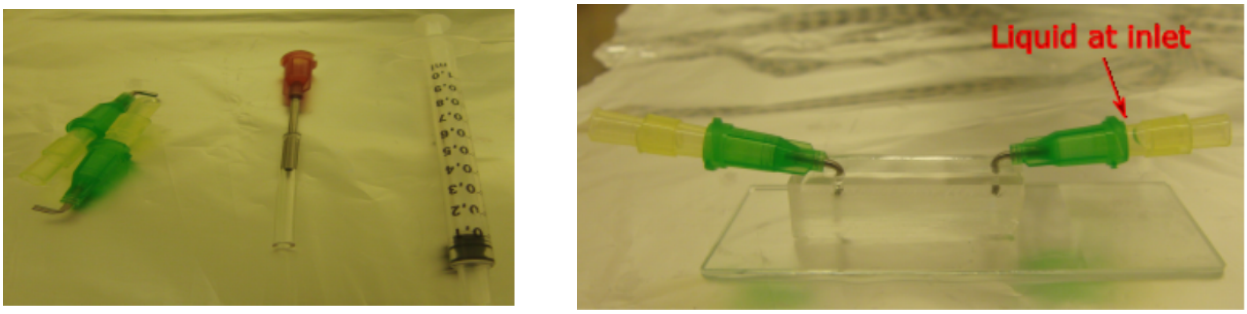

(a) (b)

Figure 3.11: Photoreactive solution preparation and loading. (**a**) From left: precission tip, adapter and 1 ml syringe (**b**) A loaded microfluidic device with liquid at inlet.

3.2.2 Photopolymerization Setup

The loaded device is then mounted on an Inverted Nikon Eclipse Ti-E microscope. Both the ends of device are connected to regular silicon tubings that are secured to the stage of the microscope using tape. We use Fluigent's all-in-one Microfluidic Flow Control System to maintain the pressure at the inlet, while the oulet is left open to atmosphere. A 130 W Nikon Intensilight mercury lamp is used as the UV light source, with the duration of the exposure controlled using a Nikon NI-SH-E shutter.

The channel filled with the prepolymer mixture of desired concentration is exposed to a pulse of UV light through a lithography mask placed in the field-stop of the microscope, fig. 3.13b. The 20× objective is used for both particle particle production and tracking. During the course of the trials, any light source (especially the ones containing UV component) within laboratory is switched off as to prevent undesired polymerization within the channels.

The movement of the particles are recorded using the Andor Zyla 4.2 sCMOS camera with a frame rate ≈18 fps. To keep track of the particle motion, the microscope stage is operated using a custom made macro.

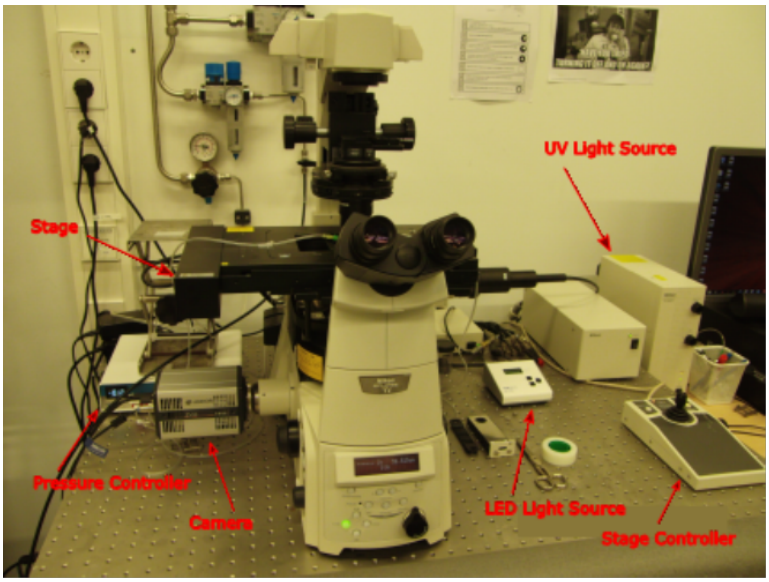

Figure 3.12: Total setup under operation. From left to right, the image consists of: stage to position the microfluidic device over the observation lens, pressure controller to regulate the inlet pressure, camera to record the observation, LED light source to illuminate the sample under observation, stage controller to control the position of the stage and UV light source connected via optical fibre to initiate the photo-polymerization.

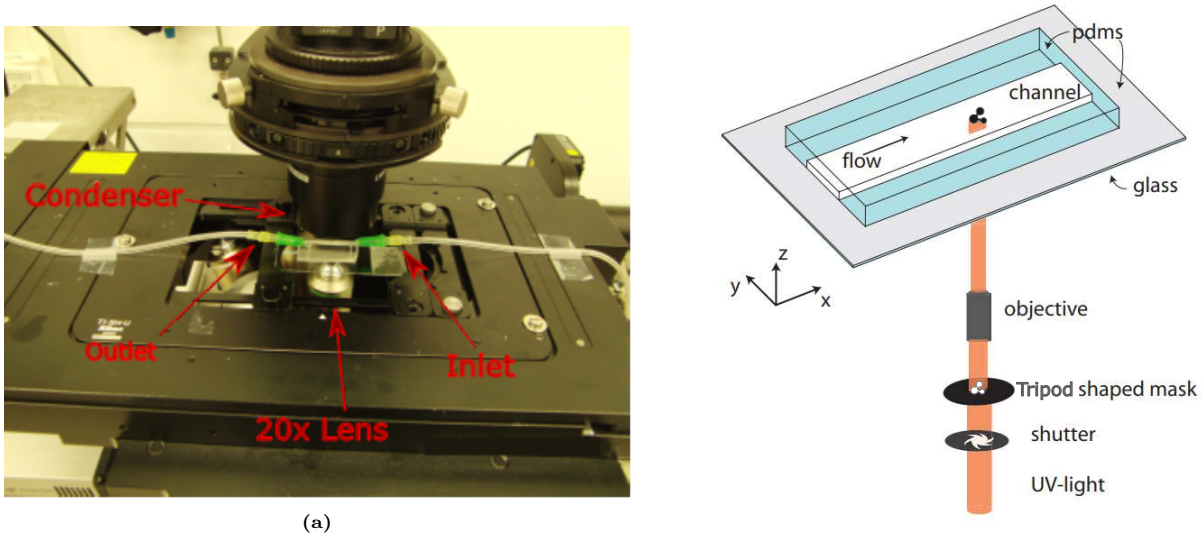

(a) (b)

Figure 3.13: Device mounting and *in situ* production of the micro-particles. (**a**) The inlet of the channel is connected to the pressure regulator while the outlet is left open to atmosphere. Condenser is used to focus the LED light over the sample for observation and recording. (**b**) Controlled UV light is projected through a tripod shaped mask onto a photo-reactive solution (source [23]).

3.2.3 Examination

3.2.3.1 Channel Height Estimation

The channel height is measured optically by finding the difference in focus between the top and bottom walls of an empty microfluidic device.

3.2.3.2 Particle Height Estimation

The height of the particles formed is dependent on polymerization conditions and the channel height. Therefore it is necessary to estimate the height as to determine the confinement ratio (β).

We first begin by forming (as shown in fig. 3.14a) particles such that the hypotenuse formed by the face width, w_1, and channel height is less that the channel height. Meaning, $\sqrt{w_1^2 + h_p^2} < H$. This condition is enough for the particle to topple over when a small flow is induced within the channel. Later, once toppled, the width of the xy - cutplane (fig. 3.14b) can be measured to assess the height.

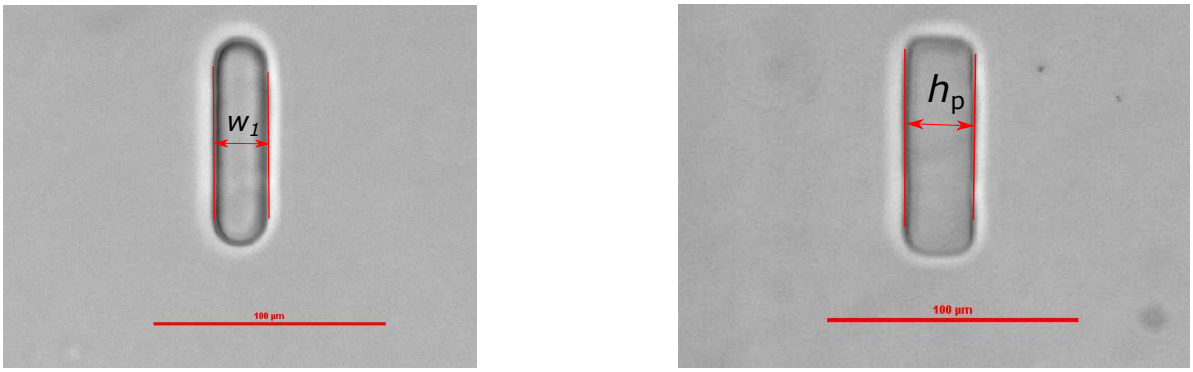

(a) (b)

Figure 3.14: Particle height estimation. (**a**) Image before toppling (soon after production) (**b**) Image of the particle after toppling. The width of the particle in the image is measured to estimate the height of the particles being formed.

3.2.3.3 Mean Flow Estimation

We begin by producing and tracking a disc shaped particle with appropriate radius. Later, the height-averaged flow velocity for an applied pressure difference is calculated using the numerical data of the corresponding disc.

$$U_0 = \frac{\text{experimentally observed disc velocity}}{\text{numerically calculated dimensionless velocity}} \tag{3.33}$$

3.2.4 Data Processing

In addition to the motion of the particle we also capture the background image - the one without the particle. In each frame we subtract the background and binarise the image for edge detection. Then we apply Hough Transform[24] to detect each disc and the channel boundaries (lines)[§]. By calculating the relative positions of the disc centres to any of the boundary we can estimate the position and orientation of the tripod with respect to the walls of the channel.

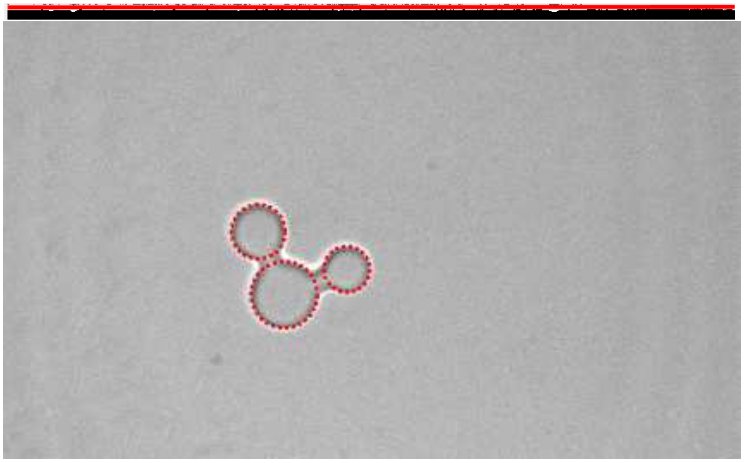

Figure 3.15: Particle tracking using Hough Transform. We detect the position of the walls and disc centres using Hough Transform for lines and circles respectively (marked in red). By knowing the relative position of the discs with respect to the wall one can calculate the position and orientation of the particle as a function of time.

[§]Hough Transform is an effective technique to process digital images having simple parametric curves such as lines, circles, etc.. By detecting the edges in the regional space (the one with image) we can plot/accumulate points in the feature space. The feature space has the curve parameters as its axes, e.g., two for lines - slope and intercept, and three for circles - centres in (x, y) and radius. By pre-deciding the shape of the expected curve each possible line (or circle) through a point detected on the edge is voted for. The parameters receiving the most number of votes is chosen for representing the edges

Chapter 4

Results and Discussion

4.1 Comparing Brinkman-2D to Stokes Quasi-2D

Here we validate the stresses on the material particle obtained using Brinkman formalism against a q2D model solved using Stokes equation. We do this by comparing the forces and torques on shapes formed by choosing different values for the parameters λ, κ, ϕ and β as seen below.

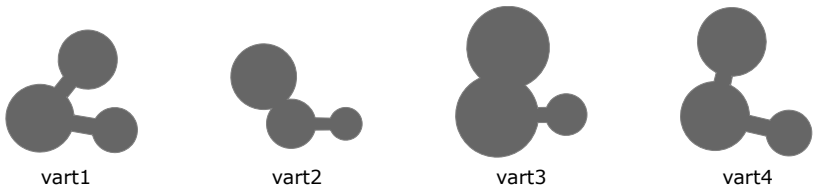

Figure 4.1: Different variants in shapes for chosen numerical study. From left, the variables in order (λ, κ, ϕ): vart1 - $(1.3, 1.5, 60°)$, vart2 - $(2, 1.5, 120°)$, vart3 - $(2, 2, 80°)$ and vart4 - $(1.5, 1.5, 90°)$.

For each of these calculations we choose the standard measurement for the elements as mentioned in fig. 3.5. The flow and particle velocities are set as $\mathbf{U}_0^* = 1\hat{i}$, $\mathbf{U}_\mathrm{p}^* = 0.5\hat{i} + 0.5\hat{j}$ and $\omega = 0.5\hat{k}$, respectively. The comparison is plotted in fig. 4.2.

Stokes q2D model

Figure 4.2d shows the mesh convergence study for the Stokes q2D model, normalised with respected to the values obtained using the current computer's maximum efficiency. The coarser to fine mesh sizes are the default options based on physics-based meshing (auto-meshing) technique incorporated in COMSOL. For the base normalization value we create a user defined mesh pattern with mesh sizes fine, fine and finer for fluid domain, particle's transversal and lateral surfaces respectively. Based on the results we choose to simulate the model with fine grids (from auto-meshing), as it is within 2 % margin and relatively takes less time to compute.

Below we compare the forces acquired using different author's approach (all using height averaged Brinkman equation) - normalised with respect to Stokes q2D, for a confinement ratio, $\beta = 0.8$. Let us go through the methods one by one:

B. Bet's Method

- In all the cases by using Bram Bet's method[14], on particle sides we get higher forces and hence torque than expected. This can be attributed to the approach of moving the body in Brinkman-2D with the same velocities prescribed to Stokes q2D. In addition, the author also assumes that the particle spans the entire channel height leading to an increased surface area on lateral sides for force integration.

- In gaps, the force $\mathbf{F}^0$ drops to zero since the simple Couette flow model implemented has zero velocity gradient in-between wall and stationary particle.

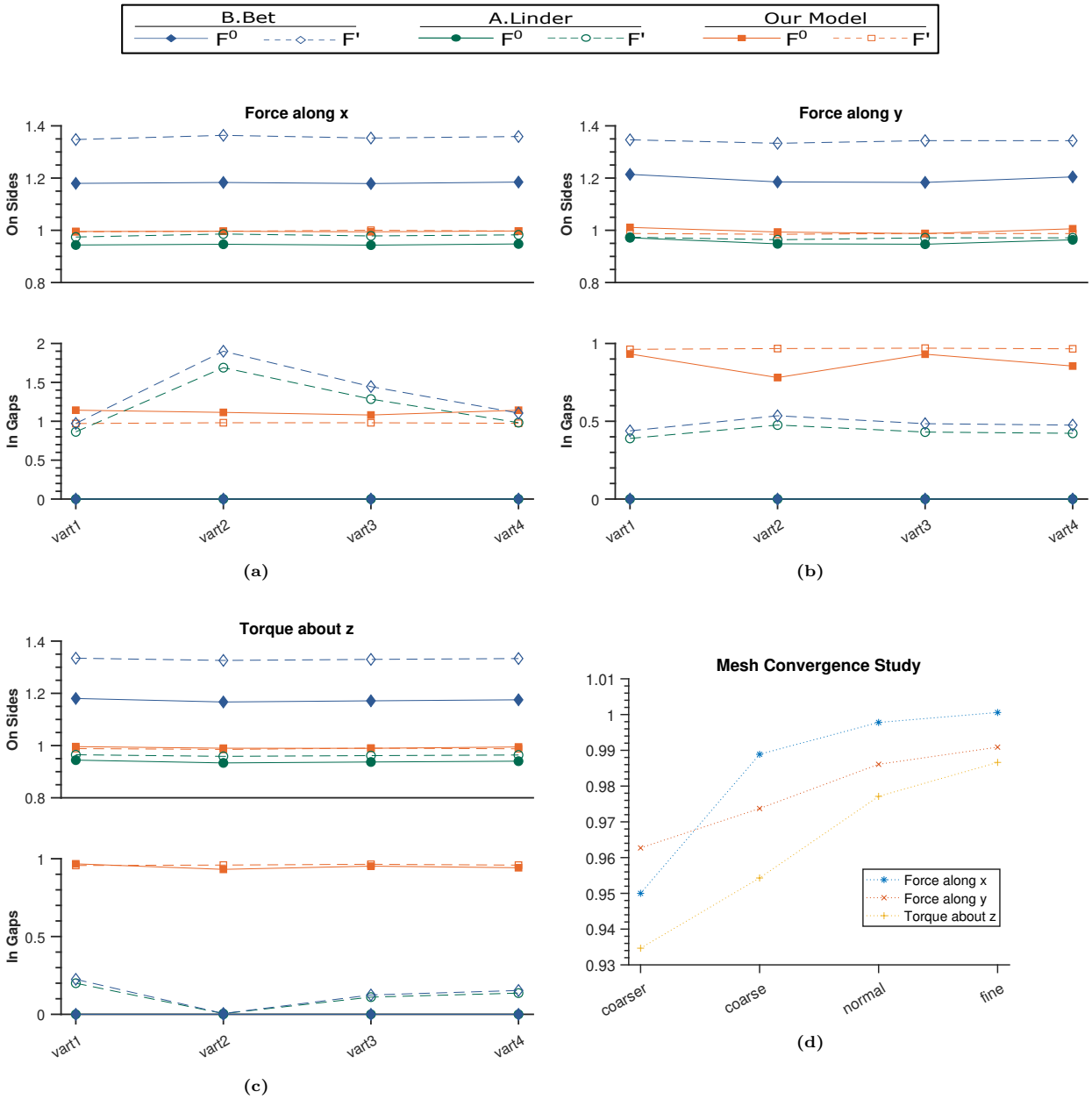

Figure 4.2: Force and torque comparison study with different authors. The confinement ratio (β) is set to 0.8 throughout this calculation. (**a**)-(**c**) For all the cases and variants, the forces and torques produced on both the lateral (horizontal side), and transversal (surface within lubrication gap) faces of the particle in our height-averaged model is in very good agreement with the solution computed using stokes equation in a q2D channel. (**d**) Grid dependence study for an q2D model solved using Stokes equation.

- In the gaps for the force $\mathbf{F}'$, its magnitude is less that expected. This is because when a particle moves in an otherwise quiescent medium, the leading face/side of the particle causes a local pressure build-up. And hence we will have a positive pressure gradient (for translation in positive x direction) contributing to increase in drag. Since this model does not account for this effect, it predicts less drag.

A. Linder's Method

- On the particle sides, the forces and hence the torque are within 10 % margin. They are consistently less since the forces are calculated by integrating the height average force over the particle boundary in Brinkman-2D. This is done in reference to eq. (3.2), though by only integrating over particle height h_p instead of H. However, the lateral side of the particle only interacts with the adjacent fluid - which has a higher magnitude than average (already covered in section 3.1.2). Thus, by using the height averaged force ($z = [0, H]$), we will face a higher deviation in lateral forces as the confinement ratio β decreases.
- In the gaps, for $\mathbf{F}'$, this model consistently predicts slightly less force than B. Bets's because it assumes a fixed composite particle's velocity profile (only function of β) in Ω_p, as shown in fig. 3.2. Thus it predicts a negative pressure gradient even though the current case has a positive gradient. Consequently, the particle experiences less drag than actual in the gaps. $\mathbf{F}^0$ is constantly zero since the composite velocity profile has zero magnitude for a stationary particle.

Our Method

As seen our model agrees well with the Stokes q2D for all the cases and variants, except for lateral force along y in vart2 and vart4. This is because the magnitude of the y force in the gaps compared to the sides is less than 15% for all variants. Thus small errors in the absolute value reflect significantly in the relative comparison. However, this does not make much of a difference in the total force on the particle since its magnitude is found to be less than 1% of the total force $\mathbf{F}^0$ for all variants.

4.2 Stable Orientation of a Moving Particle

Within an unbound q2D channel, for a moving particle suspended in a fluid stream, we can write the dimensionless instantaneous velocities at time t using eq. (3.26)

$$\begin{pmatrix} {}_t\mathbf{U}^*_\mathrm{p} \\ {}_t\omega^*_\mathrm{p} \end{pmatrix} = {}_t\mathbb{R}^r \cdot \begin{pmatrix} 1 \\ 0 \end{pmatrix} \tag{4.1}$$

Thus for any other arbitrary time, t_n, the particles resistance tensor ratio ${}_{t_n}\mathbb{R}^r$ can be represented by transforming its component tensors as follows

$${}_{t_n}\mathbb{R}^0 = \begin{pmatrix} \mathbf{Q} \cdot {}_t\mathbf{K}^0 \cdot \mathbf{Q}^\dagger \\ {}_t\mathbf{C}^0 \cdot \mathbf{Q} \end{pmatrix} \qquad {}_{t_n}\mathbb{R}' = \begin{pmatrix} \mathbf{Q} \cdot {}_t\mathbf{K}' \cdot \mathbf{Q}^\dagger & \mathbf{Q} \cdot {}_t\mathbf{C}'^\dagger \\ (\mathbf{Q} \cdot {}_t\mathbf{C}'^\dagger)^\dagger & {}_t\mathbf{\Omega}' \end{pmatrix}, \tag{4.2, 4.3}$$

in which ${}_t\mathbf{K}$ and ${}_t\mathbf{C}$ are the elements of the resistance tensor ${}_t\mathbb{R}$ and $\mathbf{Q}$ a function of the angle that the particle has rotated about centroid. To simplify the final solution, we make use of the surface mobility tensor $\mathbb{M}'$ instead of $\mathbb{R}'^{-1}$. $\mathbb{M}'$ also follows the same transformation laws as $\mathbb{R}'$. For ${}_t\tilde{\mathbf{K}}'$, ${}_t\tilde{\mathbf{C}}'$ and ${}_t\tilde{\mathbf{\Omega}}'$ being the elements of $\mathbb{M}'$,

$${}_{t_n}\mathbb{M}' = \begin{pmatrix} \mathbf{Q} \cdot {}_t\tilde{\mathbf{K}}' \cdot \mathbf{Q}^\dagger & \mathbf{Q} \cdot {}_t\tilde{\mathbf{C}}'^\dagger \\ (\mathbf{Q} \cdot {}_t\tilde{\mathbf{C}}'^\dagger)^\dagger & {}_t\tilde{\mathbf{\Omega}}' \end{pmatrix}, \tag{4.4}$$

By solving for

$$\begin{pmatrix} {}_{t_n}\mathbf{U}^*_\mathrm{p} \\ {}_{t_n}\omega^*_\mathrm{p} \end{pmatrix} = {}_{t_n}\mathbb{M}' \cdot \left\{ {}_{t_n}\mathbb{R}^0 \cdot \begin{pmatrix} 1 \\ 0 \end{pmatrix} \right\} \tag{4.5}$$

we would obtain a unique value for θ such that ω is zero. The equation for equilibrium angle, θ_eq, indeed can be expressed as

$$\tan(\theta_\mathrm{eq}) = -\left(\frac{M_{13}R^0_{11} + M_{23}R^0_{21} + M_{33}R^0_{32}}{-M_{13}R^0_{12} - M_{23}R^0_{22} + M_{33}R^0_{32}} \right), \tag{4.6}$$

where, M_{ij} and R_{ij} correspond to the elements of the respective matrices. Inherently, θ and $(\pi + \theta)$ are the stable and unstable *equilibrium angles* - the further analysis for which is discussed in section 4.6. Thus by knowing the values of the resistance tensors at a given configuration, we can immediately calculate the equilibrium angle with respect to the current orientation.

4.3 Equations of Motion

In all our future analysis we take the stable equilibrium angle, θ_{seq}, to be zero. Meaning we define the particle orientation with respect to this angle. Though this angle (θ_{seq}) is zero, the particle's angular bisector can indeed be oriented at some degree with respect to the flow direction. An visual representation of this can be seen from fig. 4.1, where the particles are in their respective stable equilibrium orientations for a stream flowing along x.

The validity of choosing $\theta_{\text{seq}} = 0$ and estimating the dynamics of the particle comes from the fact that the Stokes equation is time reversible. It is well understood by considering that at t_n the particle is oriented at θ_{seq}. Thus for any time $t \in \{(-\infty, t_n) \cup (t_n, \infty)\}$, we can transform the tensors as

$$ {}_t\mathbb{R}^0 = \begin{pmatrix} \mathbf{Q} \cdot {}_{t_n}\mathbf{K}^0 \cdot \mathbf{Q}^\dagger \\ {}_{t_n}\mathbf{C}^0 \cdot \mathbf{Q} \end{pmatrix} \qquad {}_t\mathbb{M}' = \begin{pmatrix} \mathbf{Q} \cdot {}_{t_n}\tilde{\mathbf{K}}' \cdot \mathbf{Q}^\dagger & \mathbf{Q} \cdot {}_{t_n}\tilde{\mathbf{C}}'^\dagger \\ (\mathbf{Q} \cdot {}_{t_n}\tilde{\mathbf{C}}'^\dagger)^\dagger & {}_{t_n}\tilde{\mathbf{\Omega}}' \end{pmatrix}, \tag{4.7, 4.8} $$

where $\mathbf{Q}$ is the function of the angle that the particle has rotated from θ_{seq}. The angle of rotation can either be positive or negative based on the direction of rotation. Therefore, the corresponding instantaneous force and torque free velocities at that point in time can be calculated using eq. (4.1)

$$ \begin{pmatrix} {}_t\mathbf{U}^*_{\text{p}} \\ {}_t\omega^*_{\text{p}} \end{pmatrix} = {}_t\mathbb{M}' \cdot \left\{ {}_t\mathbb{R}^0 \cdot \begin{pmatrix} 1 \\ 0 \end{pmatrix} \right\} \tag{4.9} $$

For a moving particle suspended in a fluid stream within an unbound q2D channel, we can derive the equations of motion in x and y using the equation above. A detailed derivation is presented in Supplementary Information B, from which

$$ \omega_\theta = \frac{\sin(\theta)}{\tau_\theta} \tag{4.10} $$

$$ \dot{y}_\theta = \dot{y}_\perp \sin^2(\theta) + \dot{y}_\parallel \cos^2(\theta) + (\dot{x}_\parallel - \dot{x}_\perp) \sin(\theta)\cos(\theta) \tag{4.11} $$

$$ \dot{x}_\theta = \dot{x}_\perp \sin^2(\theta) + \dot{x}_\parallel \cos^2(\theta) + (\dot{y}_\perp - \dot{y}_\parallel) \sin(\theta)\cos(\theta) \tag{4.12} $$

where $(\dot{x}_\theta, \dot{y}_\theta, \omega_\theta)$ are the velocities of the particle at any angle θ with respect to θ_{seq}, and τ_θ is the *rotation time scale* defined as the inverse of the angular velocity at orientation $\theta_{\text{seq}} + 90°$. Furthermore, $(\parallel, \perp)$ are corresponding translational velocities when oriented at $(\theta_{\text{seq}}, \theta_{\text{seq}} + 90°)$ respectively. Thus

$$ \tau_\theta = 1/\dot{\theta}_\perp \tag{4.13} $$

remember that τ_θ can either be positive or negative depending on the direction of rotation.

By integrating eq. (4.10) under the boundary condition: $t = 0$ at $\theta = \theta_{\text{seq}}$, we can solve for the angular position at any time t as

$$ \theta = 2\tan^{-1}(\exp(t/\tau_\theta)) \tag{4.14} $$

By estimating τ_θ, a unique value based on the exterior geometry of the particle, we can trace an universal behaviour for any arbitrary shape. In addition, only by knowing the $\parallel$ and $\perp$ velocities we can compute the translational velocities at any orientation. Thus given the necessary parameters for a geometry $(\tau_\theta, \dot{x}_\parallel, \dot{y}_\parallel, \dot{x}_\perp, \dot{y}_\perp)$, we can determine the complete trajectory in phase and space. To illustrate this *analytical model*, we plot the simulation results obtained using our Brinkman-2D model against the calculated *equations of motion*.

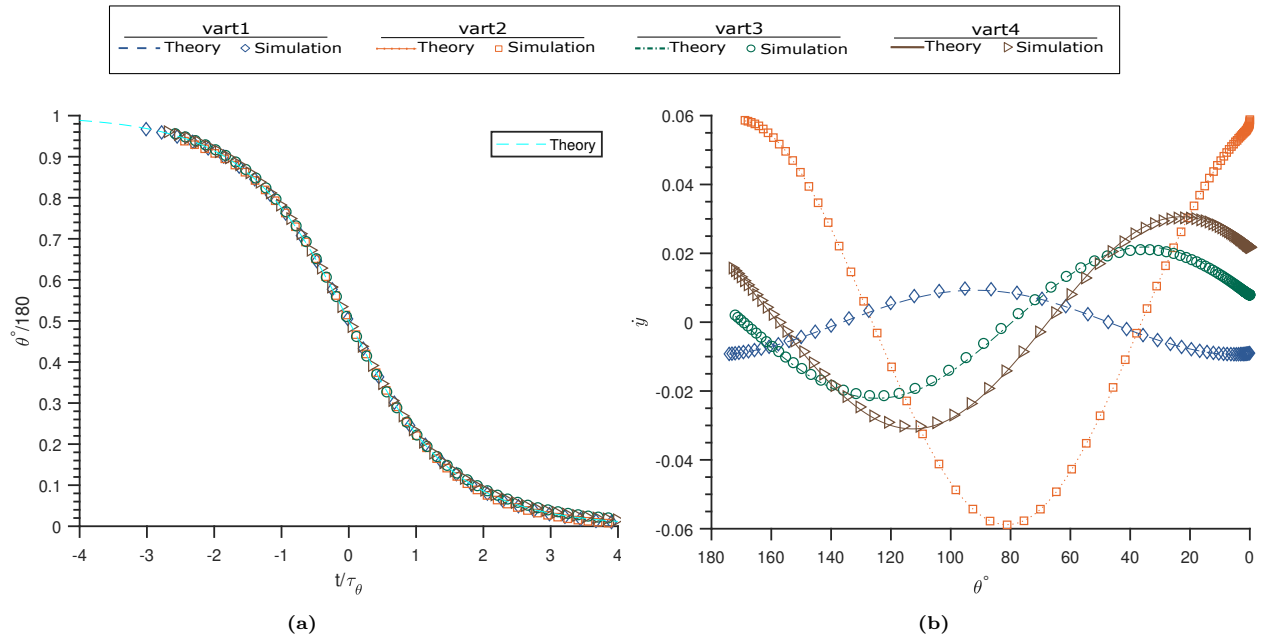

Figure 4.3: Universal behaviour of any arbitrary shaped particle. (**a**) Shows the analytical and numerical phase plot as a function of dimensionless time - scaled with the respective rotational time scales of the particle (**b**) Predicted and numerically estimated velocities of the particle along y (drift velocity) due to cross stream migration.

Figure 4.3a shows the phase plot for different variants. In all cases we initiate the particle's angular position a bit away from the unstable equilibrium orientation as to facilitate the rotation. The similarity of the curve about $t = 0$ exists because the particle behaves identically when rotated to either direction of the equilibrium angles from $\theta_{\text{seq}} + 90°$. Though the simulations were done in a laterally bounded channel with, $c/W \approx 0.2$ (c - characteristic particle dimension), we still see a very good agreement with the theory. This negligible effect of finite lateral confinement on particle trajectory can be explained using eq. (2.75)

For the q2D system under consideration, the disturbance decays as $\mathcal{O}(r^{-2})$, also seen from the mobility tensor $\mathbf{B}(\mathbf{r})$ in eq. (2.53). λ_{w} already contains this information, and in addition is an intrinsic function of l (distance from the wall to the centre of particle). Thus higher degree effects in $\lambda_{\text{w}} \sim \mathcal{O}(1/l)^m$, with $m >= 2$ degrades the significant effect of finite walls (along lateral side).

4.4 Effect of Symmetries

The general equations of motion (eqs. (4.10) to (4.12)) can be further simplified based on the symmetry planes that a geometry possesses. For all the cases below we consider a flow along x for a particle in an unbound q2D channel or far away from the lateral walls.

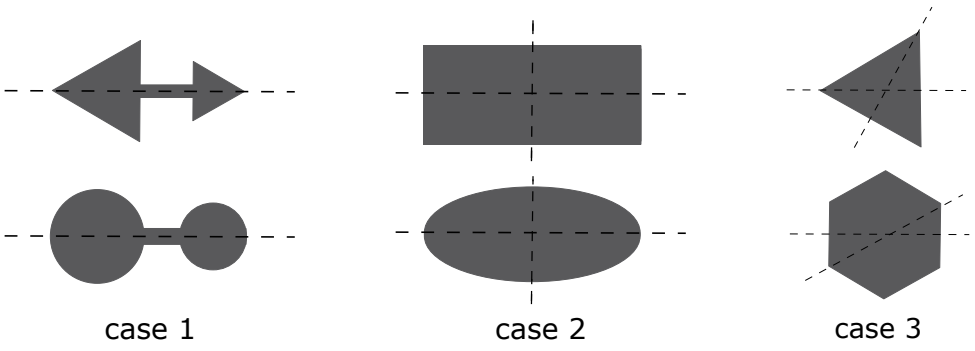

Figure 4.4: Types of symmetries in an arbitrary shape. Starting from left we have particles with one axis of symmetry, Anisotropic particles with two axis of symmetry and Isotropic particles with three or more axis of symmetry.

Case 1 : Particles with one axis of symmetry

For these cases due to the symmetry the equilibrium orientations will correspond to when the symmetry axis is parallel to the flow. Also for the same reason the velocities $\dot{y}_\perp$ and $\dot{y}_\parallel$ would be zero when oriented along the equilibrium angular position. In mathematical sense, this symmetry axis is one of the principal axes of resistance of the particle[25], with the other axis perpendicular to it - contributing to $\dot{y}_\perp = 0$.

Necessary parameters for equations of motion: $\tau_\theta, \dot{x}_\parallel, \dot{x}_\perp$

Case 2 : Particles with two axis of symmetry (Anisotropic)

Due to the dual symmetry of the shapes like rectangle and ellipse, their geometric centroid is also the centre of hydrodynamic stress. Which means that the coupling tensor about centroid is zero - creating no torque due to translation. Due to the nature of the Stokes flow the net torque on the particle at any instant should be zero, and hence the torque generated by rotation should be zero ($\omega = 0$). Therefore, a particle has infinite number of stable orientations. However the particle would drift along y[23] as a result of unequal eigenvalues (for translation) along principal axes.

Necessary parameters for equations of motion: $\dot{x}_\parallel, \dot{x}_\perp$

Case 3 : Particles with minimum three axis of symmetry (Isotropic)

These are the special cases of anisotropic bodies where the eigenvalues for the translational resistance tensor are equal. Meaning, when transformed to any angle they would again produce a diagonal matrix - the off-diagonal components which contribute to the drift are zero. Hence, these geometries, in addition to infinite stable orientations would also have zero drift for all orientations.

Necessary parameters for equations of motion: $\dot{x}_\parallel = \dot{x}_\perp = \dot{x}$

4.5 Experimental Results

In order to further validate the computational results and theory we compare them to the experimental data obtained.

The experiment is performed by supplying a pressure difference of 5 mbar across the channel. All the particles are produced with an exposure time of 0.1 s, while the focus positioned at distance -20 µm from the bottom wall ($z = -20$ µm). The UV light intensity is set to ND1, standard scale from Nikon's 130 W mercury lamp.

A disc with radius 36 µm was tracked to estimate the height averaged velocity U_0. The velocity of the disc was measured to be 62.7 µms^{-1} in a channel of 33 µm heigh, and the particle height was measured to be 29$\pm$ 0.5 µm by flipping the pill particles (fig. 3.14b). Thus, for a confinement ratio of 0.88 the dimensionless velocity (U_p/U_0) of the disc was numerically computed to be 0.6647. Using the above values we estimate the mean flow $U_0 = 94.33\,\mu$ms^{-1}. Below are the results.

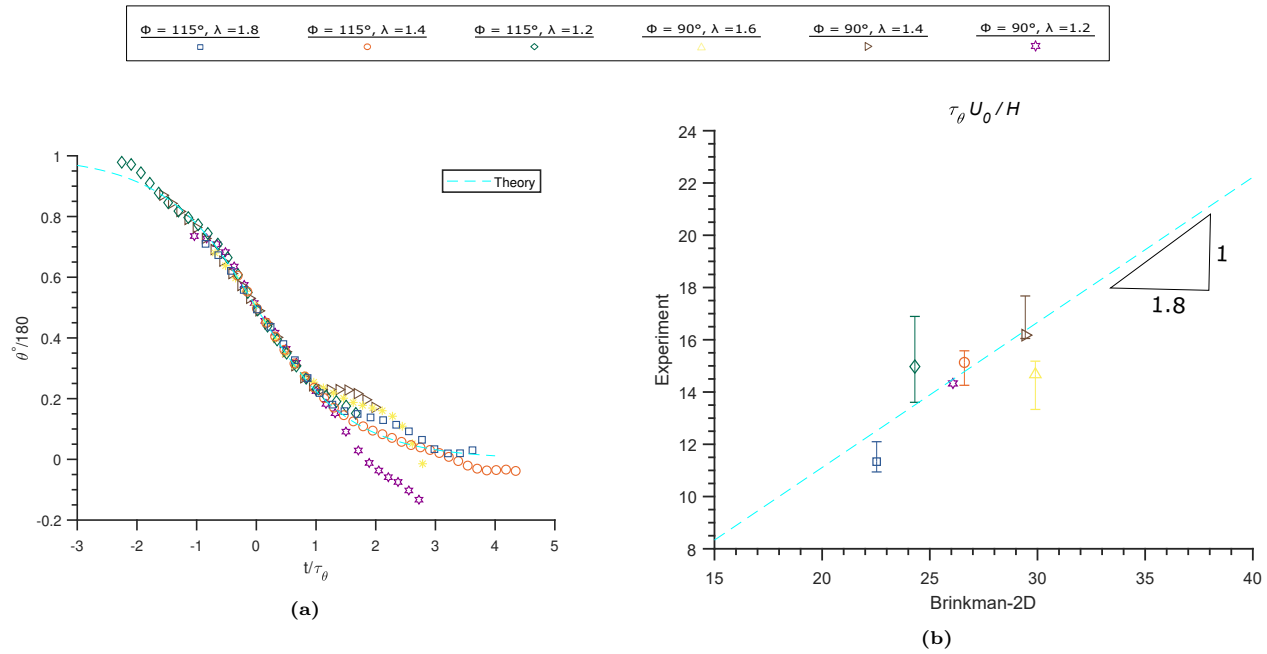

Figure 4.5: Rotational response of particles recorded using experiment. (**a**) The experimental phase plot of different geometries matched against the proven analytical model. In some cases, deviations in the data is found at angles close to stable equilibrium orientation. Since the angular velocity is comparatively less at these angles (can be explained using sine based correlation, eq. (4.10)), even a small perturbation due to channel defects affect the particle dynamics (**b**) Plot containing the dimensionless rotational time scale from experiments plotted against the numerically computed values. The data is found to closely match when the experimental values are scaled up by a factor of 1.8

As seen from fig. 4.5a, in the vicinity of $t = 0$ for all the geometries the plots match very well to the theory/simulation. However, close to the stable orientation ($\theta = 0°$) we see a deviation from the prediction. In the range of equilibrium orientations ($\theta = 0°\text{or}180°$) the angular velocities for any geometry is minimum, refer eq. (4.10). Thus, any small perturbations due to channel irregularities is more pronounced close to the equilibrium angles. On the contrary, when oriented at $\theta = 90°$ the particles attain the maximum rotational velocity, making the disturbances less significant. The method by which $t = 0$ and τ_θ are calculated from the experimental results is mentioned in Supplementary Information C

4.6 Physical Inference

In the previous sections we saw that a particle has a stable and an unstable equilibrium orientations, and how these angular positions help us correlate the general dynamics of the particle. Here we try to explain the physical meaning behind these orientations.

For a particle in an unbound and unconfined medium (both the lateral and transversal walls at infinity respectively), a particle would posses only one resistance tensor. We have seen how a q2D channel gives rise to two resistance tensors corresponding to flow and particle velocities respectively. Thus, for q2D cases one should obtain two centres of hydodynamic stress, (C^0, C'), calculated using each individual resistance tensors $\mathbb{R}^0$ and $\mathbb{R}'$. Although the centre of hydrodynamic stress need not always exist [13], for a particle in 2D it always exists. The simple explanation would be that for a particle about its centre of reaction (which always exists and is unique), the coupling tensor $\mathbf{C}$ should be symmetric. For a q2D case since we have only a 1×2 matrix instead of 3×3, this would only mean that $\mathbf{C} = 0$ - a condition for the centre of hydrodynamic stress. The centres C^0 and C' can be found by solving the simplified form of the eq. (2.24) as follows

$$\begin{pmatrix} -y_{C^0} \\ x_{C^0} \end{pmatrix} = (\mathbf{K^0})^{-1} \cdot (\mathbf{C^0})^\dagger, \qquad \begin{pmatrix} -y_{C'} \\ x_{C'} \end{pmatrix} = (\mathbf{K'})^{-1} \cdot \mathbf{C'}^\dagger, \tag{4.15a, 4.15b}$$

where (x, y) are the positions of the respective centres of hydrodynamic stress relative to geometric centroid

of the particle. To visualise the above mentioned we consider a dumbell with one axis of symmetry (see below).

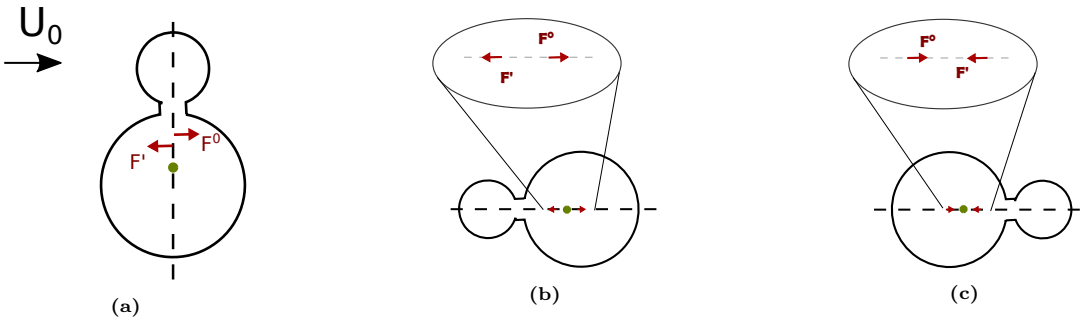

Figure 4.6: Detailing orientational stability. In all the above figures the geometric centroid of the particle is marked using a green dot, and the position and force acting on the centres of the hydrodynamic stress is represented using the red arrow. (**a**) Particle positioned at $+90°$ to the stable orientation (**b**) Particle at its unstable equilibrium orientation (**c**) The stable angular configuration of the particle

In fig. 4.6a, for the particle oriented at $90°$ with respect to its stable angle, the positions of C^0, C' and direction of the force acting on them are displayed. Due to the nature of the forces, $\{\mathbf{F}^0\}_x$ would always point towards flow direction, while $\{\mathbf{F}'\}_x$ would have direction opposite to the flow. Due the symmetry of the geometry considered above one can explain the forces $\mathbf{F}^0$ and $\mathbf{F}'$ having only the x component when the axis of symmetry is aligned with the flow. Thus, the torque produced by either of the resistance tensors is zero since the geometric centroid lies in the same axis (angle between the forces and the position vectors of C^0 or C' relative to centroid is either $0°$ or $180°$). Hence both of these orientation correspond to the equilibrium angle, while fig. 4.6c gives the stable orientation. In principle for a particle to have zero rotational velocity, for a purely translating body the net torques produced by the equivalent point forces (acting on C^0 and C') about geometric centroid should be zero. Although the resistance tensors $\mathbb{R}^0$ and $\mathbb{R}'$ determine the positions of the centres of hydrodynamic stress, the magnitude and direction of the force acting on them is determined together with fluid velocity for $\mathbf{F}^0$ and particle velocity for $\mathbf{F}'$, respectively.

Below we illustrate the positions of C^0 and C' for a more complex geometry when oriented along the stable equilibrium angle

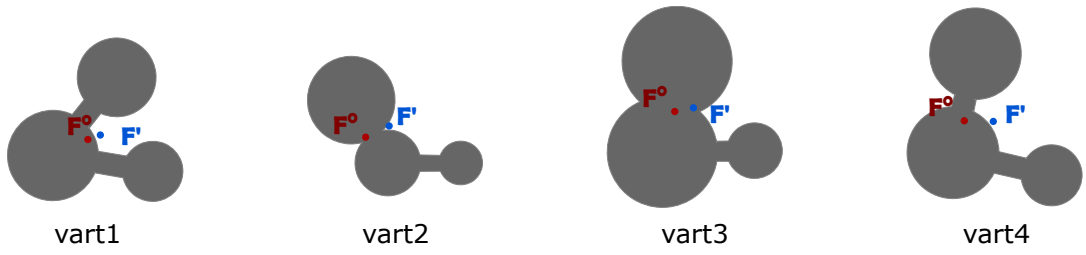

Figure 4.7: Position of the Centres of the Hydrodynamic Stress. The image shows the positions of the centres of the hydrodynamic stress for the respective particles when oriented along their stable equilibrium angle. The centres due to $\mathbf{F}^0$ and $\mathbf{F}'$ are marked with red and blue respectively.

Chapter 5

Summary and Recommendations

5.1 Summary

Low Reynolds flows in shallow channels had found its applicability in both theoretical and experimental fields due to the simplistic solution to the governing equations and reduced number of degrees of freedom in the system. In the present work, we have focused on explaining the universal behaviour of particles with any arbitrary shape, sufficiently far from the horizontal bounding walls (in lateral direction), by combining analytical, numerical and experimental techniques.

The dynamics of the particles are dependent only on the exterior geometry, and therefore is independent of the fluid properties. Thus, the *self-steering* ability of the particles can be harnessed by studying the effect of geometry on particle motion. We began by introducing the concept of resistance tensors and their properties for a particle suspended in an infinite medium (unbound and non-confined). Later, we restrict ourselves to a quasi-2D system and discuss the effect of momentum screening due to the parallel confining walls (in transversal direction) on the force and torque matrix. The transformations laws for the resistance tensors of a particle with reduced degrees of freedom in an unbound q2D flows, as explained in chapter 2 serves as the basis for the analytical solution to the general equations of motion. In the end of chapter 2, we derive the two dimensional translational tensor (in reference to [18]) for a finite medium as to have an overview on the effect of transversal walls on a particle placed at sufficiently large distance from them.

In chapter 3, for our numerical model we makes use of COMSOL to solve the depth-averaged 2D Brinkman equation, derived for the Stokes flow in a Hele-Shaw cell. Although the Brinkman formalism solves for the depth-averaged pressure and velocity fields in 2D, our particles don't occupy the entire height of the channel. Therefore, due to the parabolic fluid velocity profile along height, it is necessary to calculate the effective momentum transferred from fluid to particle only at the places where the material particle is present. We approach this problem by considering *composite particles* in a 2D environment, introduced in [19]. Despite the fact that the former treatment of the particles have been applied to the rectangle shaped fibres, we extended the utilization of the ansartz to complex geometries. However, we differ by treating the suggested flow profile in regions very close to the particle's lateral surface, rather than to the velocities above and below the particles. We model the flows in the gaps (lubricating layer separating the particle and transversal walls) using decoupled Couette flows along x and y directions. We take advantage of MATLAB to model the forces in the gaps. These gap forces can be a consequence of both the shear flows due to the particle motion and due to the existence of the pressure difference across the particle. Thus, we estimate the boundary points on the geometry by drawing coils of straight grills, both parallel and perpendicular to the flow, as to calculate the pressure gradients in x and y. Using the established numerical framework, we solve for the given orientation and position of the particle to compute its resistance tensors about its geometric centroid. Thereafter, utilizing these resistance tensors we solve for the instantaneous force and torque free velocities of the particle. An first order kinematic equation is employed to calculate the relative position and orientation of the particle at next time step. Henceforth, this cycle is repeated by starting again with solving the quasi-steady model, finding the velocities and positioning the particle for next time step. By doing so we get the complete trajectory of a body simultaneously translating and rotating in a flow induced by pressure difference across the channel ends.

Experiments were performed by producing mask-defined shapes of micro-particles, using the *stop-flow lithography* technique within a shallow micro-channel containing pre-polymer solution. SFL uses the science behind the free radical photo-polymerizations to form *in situ* "free-standing particles", having a symmetrical lubrication layer at top and bottom of the particle. The particle heights were measured by forming thin rectangular fibres sufficient enough to topple under flow conditions. The channel heights were measured optically using the microscope. The height-averaged flow was estimated by correlating the experimentally observed disc velocities to the dimensionless velocity obtained using numerical simulation. The experimental data was processes by performing linear and circular Hough Transform for the channel walls and particles respectively. The positions of the centre of the discs with respect to the walls is used to calculate the relative position and orientation at any instant in time.

In chapter 4 we compare our model (employing the 2D Brinkman formalism), to those by Bet and Linder and benchmark their accuracy against the q2D model solved using the Stokes equations. The model we propose agrees well with the q2D model when compared to the existing models. Thereafter, we estimate the equilibrium orientations of any arbitrary shape only from the knowledge of resistance tensors, by analytically solving the equation using their properties for transformation. Accordingly, we plot the phase and drift velocity (due to cross-steam migration) trajectories for four randomly chosen arbitrary shapes. The plots or the trajectories are found to be in excellent agreement with each other. Thus we establish an universal behaviour for asymmetric particles sufficiently far away from the walls by knowing its characteristic coefficients: one for rotation and four for translation. These coefficient reduce in numbers based on the number and nature of symmetry present in the geometry. Furthermore, to support both the matching analytical and numerical results, we verify the phase plot against experimental data. The particles are in very good agreement in the regions where they possess high angular velocities - perpendicular to the equilibrium orientations. However, close to the stable angle for few cases we find a deviation in the plot. This is because, the disturbance due to the imperfections in the channel is more pronounced at low angular velocities. The rotational timescales obtained numerically overestimate the experimental timescales by a factor of 1.8. This discrepancy in the data could be due to a number of reasons as discussed in Supplementary Information D. Finally, we provide the physical inference on the dynamics of equilibrium orientations.

5.2 Recommendations

Though the general behaviour of an arbitrary particle is discussed in the current work, the applicability of the physics to the process industries is not covered. The following recommendations are considered to be the extension of the current work:

- Selective separation: The ability of the asymmetric particles to drift cross steam even after achieving the stable orientation finds its application exclusively to the separation technologies. Thus by placing secondary outlets on the channels side walls one can effectively collect different shapes at different positions. However this would involve the study of particle dynamics at distances very close to the lateral walls.
- Short ranged multi-particle interactions: The rotational and translational coefficients/timescales should be extended to multi-particle system. For example, a phase-locked system that rotates in synchrony.
- Inertial limit: Although we deal only within the creeping flow limit, we can check for the validity of the estimated time-scales near inertial limit, since the flow around $Re \sim 1$ can be modelled using Oseen Drag - a linearised form of governing equation involving inertial component.
- Skew-symmetry Particles: Particles that become identical to itself when rotated by 180° about its geometric centroid, but lacks a plane of symmetry. A sample plot with numerically computed trajectories for a Z shaped particle is displayed in fig. 5.1.

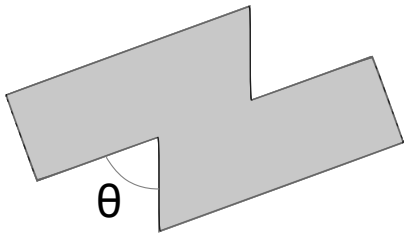

(a)

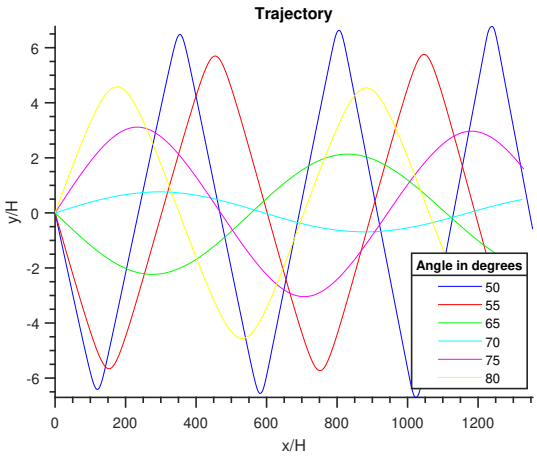

(b)

Figure 5.1: Skew Symmetric Particles. (**a**) The shape chosen to numerically simulate the trajectories (**b**) Trajectory of the centroid of a skew symmetric particle under consideration with variable geometric angle.

Acknowledgement

First and foremost, I would like to express my special thanks to my supervisors Dr. Burak Eral and Rumen Georgiev, Msc. who gave me the opportunity to work on this challenging topic.

Furthermore, my sincere gratitude to Rumen for training me in the experiments and Burak for sharing his experience. I would like to thank my other team mates Ms. Yeabsira Sahlemariam and Ms. Jess Aduana for creating a pleasant work environment.

Finally, I would also like to thank my parents, sister, and friends for supporting my career choices.

Nagaraj Nagalingam
Delft, October 2019

Supplementary Information

Supplementary Information A

Stokes linearity

Let ($\grave{\mathbf{v}}$, $\grave{\mathbf{\Pi}}$) and ($\grave{\grave{\mathbf{v}}}$, $\grave{\grave{\mathbf{\Pi}}}$) be the velocity and stress fields corresponding to any two fluid velocity vectors which conform to the stokes equations. For these two distinct fluid motions induced by a translating body, the Lorentz Reciprocal Theorem results in

$$\iint_{S_\mathrm{P}} \grave{\grave{\mathbf{v}}} \cdot \grave{\mathbf{\Pi}} \cdot d\mathrm{S} = \iint_{S_\mathrm{P}} \grave{\mathbf{v}} \cdot \grave{\grave{\mathbf{\Pi}}} \cdot d\mathrm{S} \tag{A.1}$$

Thus the force experienced by the particle in consequence of its individual motions is,

$$\mathbf{F} = \iint_{S_\mathrm{P}} \mathbf{\Pi}.d\mathrm{S} \tag{A.2}$$

For translation motion this leads to the reciprocal relation

$$\grave{\grave{\mathbf{U}}} \cdot \grave{\mathbf{F}} = \grave{\mathbf{U}} \cdot \grave{\grave{\mathbf{F}}} \tag{A.3}$$

The above equality indicates that the $\mathbf{F}$ is a linear vector function of $\mathbf{U}$. To prove this, we consecutively move the body with velocities $\mathbf{U}_1$, $\mathbf{U}_2$ and $(\mathbf{U}_1 + \mathbf{U}_2)$, and it follows from the above equation that,

$$(\mathbf{U}_1 + \mathbf{U}_2) \cdot f(\mathbf{U}_1) = \mathbf{U}_1 \cdot f(\mathbf{U}_1 + \mathbf{U}_2) \tag{A.4}$$

and

$$(\mathbf{U}_1 + \mathbf{U}_2) \cdot f(\mathbf{U}_2) = \mathbf{U}_2 \cdot f(\mathbf{U}_1 + \mathbf{U}_2), \tag{A.5}$$

where f is a function in velocity. Upon adding and rearranging the former two equations,

$$(\mathbf{U}_1 + \mathbf{U}_2) \cdot [f(\mathbf{U}_1 + \mathbf{U}_2) - f(\mathbf{U_1}) - f(\mathbf{U_2})] = 0 \tag{A.6}$$

Since the velocities $\mathbf{U}_1$ and $\mathbf{U}_2$ are arbitrary, therefore,

$$f(\mathbf{U}_1 + \mathbf{U}_2) = f(\mathbf{U_1}) + f(\mathbf{U_2}) \tag{A.7}$$

The above relation can be proved in a similar way for the rotation. Thus, the force on a particle having a combined translation and rotation can be calculated using linear relations to its velocities. The linearisation of the Stokes flow is also demonstrated using COMSOL finite-element simulations. Below in fig. A.1a we have a stationary particle suspended in a fluid stream with velocity 1. In fig. A.1b we have a particle moving with velocity 0.5 in an otherwise quiescent fluid. By summing up both of these individual fluid velocity fields, we prove that it is equal to the solution to a system have flow and particle velocities 1 and 0.5, respectively. We plot a colour map in x, y to show the difference in the solutions (refer fig. A.2).

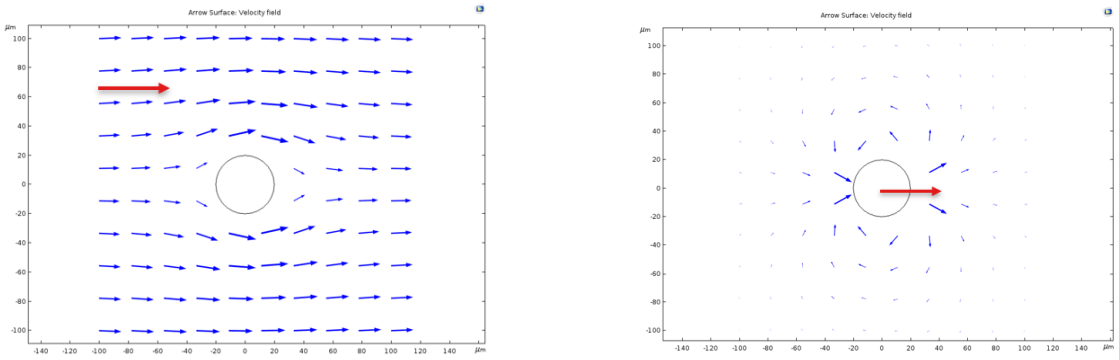

(a) (b)

Figure A.1

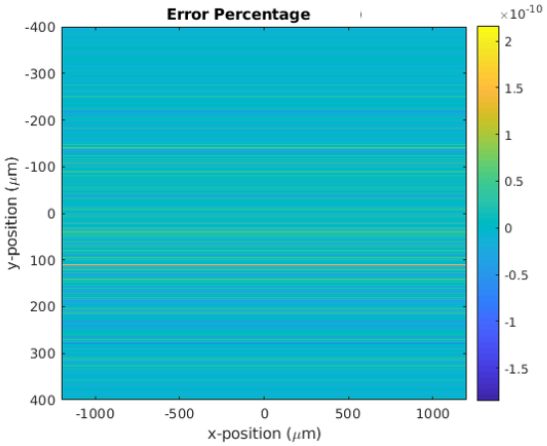

Figure A.2

Supplementary Information B

Equations of Motion - Analytical Model

For a particle suspended in an unbound quasi-2D channel, at time equals infinity the particle's orientation should attain a stable equilibrium angle. For reference we take this angle as zero. The resistance tensor at this orientation can be expressed as,

$$ {}_{t\to\infty}\mathbb{R}' = \begin{pmatrix} \mathbf{K}^0 \\ \mathbf{C}^0 \end{pmatrix} \qquad {}_{t\to\infty}\mathbb{R}' = \begin{pmatrix} \mathbf{K}' & \mathbf{C}'^{\dagger} \\ \mathbf{C}' & \mathbf{\Omega}' \end{pmatrix} \tag{B.1} $$

The resistance tensor of the same particle at any arbitrary orientation, θ, can be calculated by transforming the known resistance tensor.

$$ \mathbb{R}^0 = \begin{pmatrix} \mathbf{Q}\cdot\mathbf{K}^0\cdot\mathbf{Q}^{\dagger} \\ \mathbf{C}^0\cdot\mathbf{Q} \end{pmatrix} \qquad \mathbb{R}' = \begin{pmatrix} \mathbf{Q}\cdot\mathbf{K}'\cdot\mathbf{Q}^{\dagger} & \mathbf{Q}\cdot\mathbf{C}'^{\dagger} \\ (\mathbf{Q}\cdot\mathbf{C}'^{\dagger})^{\dagger} & \mathbf{\Omega}' \end{pmatrix}, \tag{B.2, B.3} $$

There is no angular transformation involved for $\mathbf{\Omega}$ since it is a scalar quantity in our system of consideration. In the stoke regime, due to the instantaneous dissipation of energy, the net force acting on a particle at any given space and time is zero. Thus,

$$ \begin{pmatrix} \mathbf{F} \\ \mathbf{T} \end{pmatrix} = \mu\mathbb{R}^0\cdot\mathbf{U}_0 - \mu\mathbb{R}'\cdot\begin{pmatrix} \mathbf{U}_p \\ \omega \end{pmatrix} = \begin{pmatrix} 0 \\ 0 \end{pmatrix}, \tag{B.4} $$

The mobility tensor, $\mathbb{M}' = \mathbb{R}'^{-1}$, is at the surface of the particle and obeys the same transformation laws as $\mathbb{R}'$.

$$ \begin{pmatrix} \mathbf{U}_p \\ \omega \end{pmatrix} = \mathbb{M}'\cdot\mathbb{R}^0\cdot\mathbf{U}_0 \tag{B.5} $$

Considering the stream flow to be unidirectional in x, we directly solve the above expression to get the following equation for the angular velocity at any orientation θ with respect to the stable orientation.

$$ \omega_\theta = \cos(\theta)\,(M'_{13}R^0_{11} + M'_{23}R^0_{21} + M'_{33}R^0_{32}) + \sin(\theta)\,(-M'_{13}R^0_{12} - M'_{23}R^0_{22} + M'_{33}R^0_{32}), \tag{B.6} $$

where M_{ij} and R_{ij} are the elements of the corresponding tensors. By applying the conditions at $t = \infty$, $\theta = 0$ and $\omega = 0$, we get,

$$ (M'_{13}R^0_{11} + M'_{23}R^0_{21} + M'_{33}R^0 32) = 0 \tag{B.7} $$

and, for $\theta = 90^\circ$

$$ \omega_{90^\circ} = (-M'_{13}R^0_{12} - M'_{23}R^0_{22} + M'_{33}R^0_{32}) \tag{B.8} $$

Therefore, by using eqs. (B.7) and (B.8) in eq. (B.6)

$$\omega_\theta = \omega_{90^\circ}\ \sin(\theta) = \frac{\sin(\theta)}{\tau_\theta}, \tag{B.9}$$

where, $\tau_\theta = 1/\omega_{90^\circ}$. Similarly, the translational velocities for parallel ($\parallel \widehat{=}\ \theta = 0^\circ$) and perpendicular ($\perp \widehat{=}\ \theta = 90^\circ$) configurations can be derived from eq. (B.5)

$$\begin{aligned}\dot{y}_\theta =& \sin^2(\theta)\,(M'_{11}R^0_{12} - M'_{12}R^0_{22} + M'_{13}R^0_{32}) + \cos^2(\theta)\,(M'_{21}R^0_{11} + M'_{22}R^0_{21} + M'_{23}R^0 31)\\ &+ \sin(\theta)\cos(\theta)\,(M'_{11}R^0_{11} - M'_{22}R^0_{22} + M'_{13}R^0_{31} + M'_{23}R^0_{32})\end{aligned} \tag{B.10}$$

$$\dot{y}_\theta = \sin^2(\theta)\,\dot{y}_\perp + \cos^2(\theta)\,\dot{y}_\parallel + \sin(\theta)\cos(\theta)(2\dot{y}_{45^\circ} - \dot{y}_\perp - \dot{y}_\parallel) \tag{B.11}$$

and for x velocity,

$$\begin{aligned}\dot{x}_\theta =& \sin^2(\theta)\,(M'_{21}R^0_{21} + M'_{22}R^0_{22} - M'_{23}R^0_{32}) + \cos^2(\theta)\,(M'_{21}R^0_{21} + M'_{11}R^0_{11} + M'_{13}R^0_{31})\\ &+ \sin(\theta)\cos(\theta)\,(-M'_{11}R^0_{12} - M'_{21}R^0_{11} - M'_{21}R^0_{22} - M'_{22}R^0_{21} + M'_{13}R^0_{32} - M'_{23}R^0_{31})\end{aligned} \tag{B.12}$$

$$\dot{x}_\theta = \sin^2(\theta)\,\dot{x}_\perp + \cos^2(\theta)\,\dot{x}_\parallel + \sin(\theta)\cos(\theta)\,(2\dot{x}_{45^\circ} - \dot{x}_\perp - \dot{x}_\parallel) \tag{B.13}$$

From the above set of eqs. (B.11) and (B.13),

$$2\dot{y}_{45^\circ} = \dot{y}_\perp + \dot{y}_\parallel + \dot{x}_\parallel - \dot{x}_\perp \tag{B.14}$$

$$2\dot{x}_{45^\circ} = \dot{x}_\perp + \dot{x}_\parallel + \dot{y}_\perp - \dot{y}_\parallel \tag{B.15}$$

Thus the translation velocities of an arbitrary particle as a function of orientation can be represented as,

$$\dot{y}_\theta = \sin^2\theta\,\dot{y}_\perp + \cos^2\theta\,\dot{y}_\parallel + \sin\theta\cos\theta(\dot{x}_\parallel - \dot{x}_\perp) \tag{B.16}$$

$$\dot{x}_\theta = \sin^2\theta\,\dot{x}_\perp + \cos^2\theta\,\dot{x}_\parallel + \sin\theta\cos\theta\,(\dot{y}_\perp - \dot{y}_\parallel) \tag{B.17}$$

Supplementary Information C

Estimating $t = 0$ and Calculating τ_θ

Consider the experimental plot in fig. C.1a generated using the particles with $\phi = 115°$, $\kappa = 1.5$ and $\lambda = 1.8$.

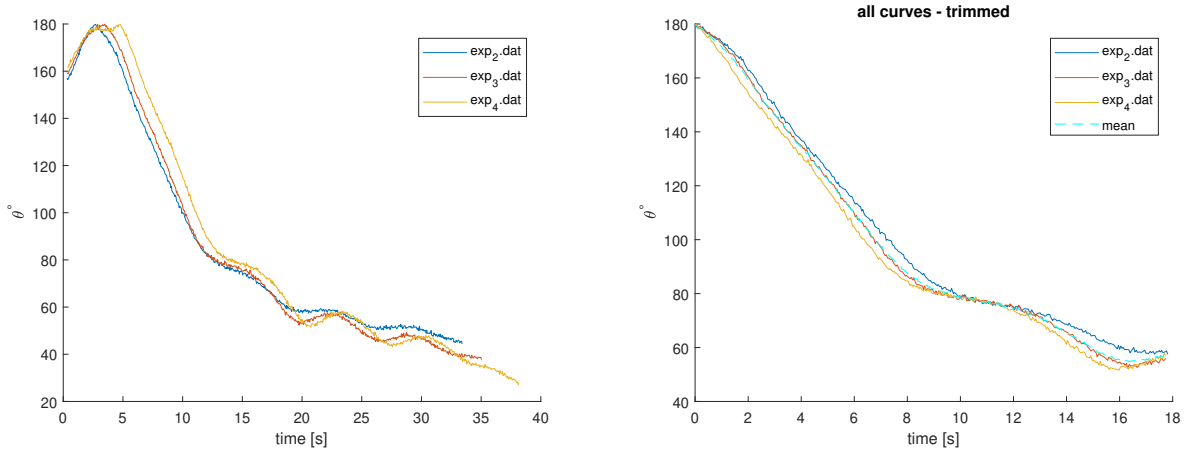

(a) **(b)**

Figure C.1

At time less than 5 sec we can see an increase in the angle, while the peak is at different time for different particles. This happens immediately after the pressure is supplied to the channel. Hence first we eliminate the time difference in the start of the actual rotation. We do this by first manually entering the time corresponding to the peaks into the MATLAB code. Each of these points is then chosen as the initial $t = 0$ to effectively trim the flow development regime, fig. C.1b. In addition, we also trim the right end based on the smallest dataset. This is done to have an equivalent number of data points for all trials, using which we can calculate the mean at every instances in time. Figure C.1b displays a mean curve plotted using a dashed line.

The calculated mean curve is smoothened by curve fitting a polynomial of order 5, see fig. C.2a. This especially is done to find the slope $\partial_t\theta$, which is the angular velocity at an orientation and time (fig. C.2b). We know from the general equations of motion (eq. (4.10)) that the angular velocity follows a sine profile. Thus, the magnitude of the rotational velocity is maximum at the point when the particle is oriented at 90° to the stable orientation. This point also corresponds to the $t = 0$ in the generalised phase plot for all shapes, refer fig. 4.3a. Thus by determining the global extremum (depending on the rotational direction), we can estimate the corresponding time which then should be taken as zero. We then subtract this value of time from the time axis, and then divide the resultant values by the rotational time scale calculated using the global extremum of the angular velocity plot.

Finally we plot the mean curve (without polynomial fit) against the dimensionless time axis (fig. C.3).

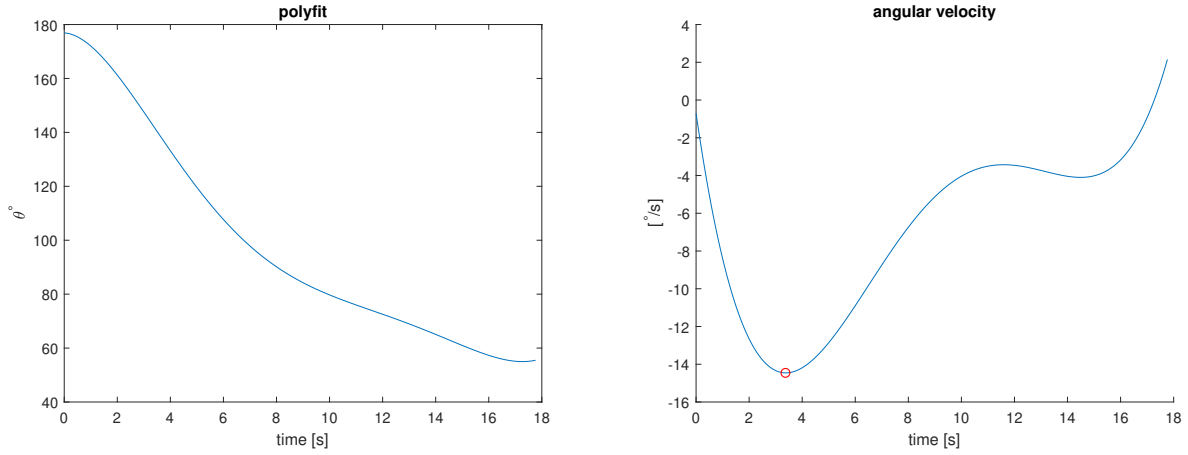

(a) **(b)**

Figure C.2

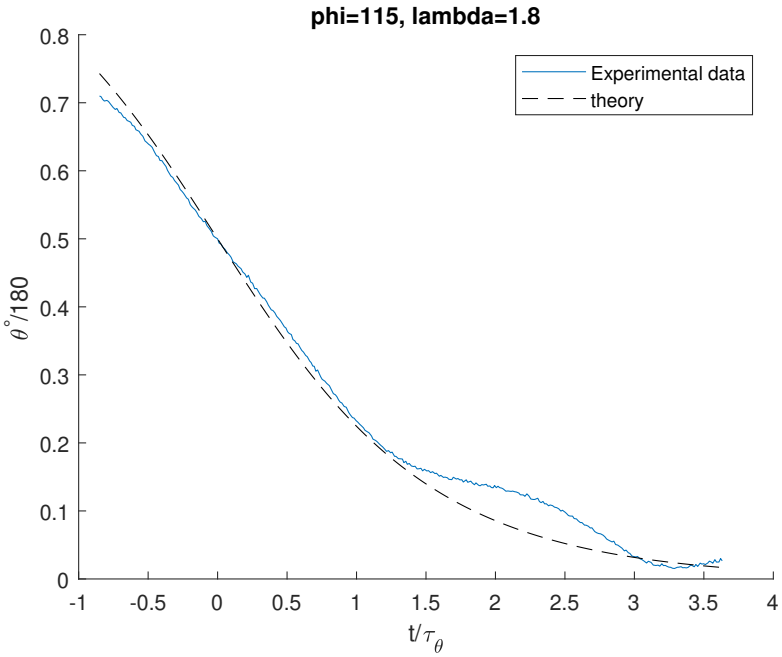

Figure C.3

Supplementary Information D

Experimental Setbacks

As mentioned in the Experimental Techniques we use 33 µm high channels with thick glass slides. Thin slides (cover slips) were not used since it made the device fragile and difficult to handle. However, for thin ones, the particles produced via SFL were found to be well defined when compared to thick slides. One reason might be due to the attenuation of the UV light within the thick ones. Also, one might expect a higher refraction due to increased thickness, which would have adverse effect on the particle's definition.

For this work, we have studied particles with very high confinement ratios ($\beta \sim 0.88$) than initially planned ($\beta \sim 0.80$). The reason being that it was difficult to differentiate the contrast on particle boundaries for the later confinements, making it hard to process the images. Also, higher the confinements, less is the stability of the particle due to channel imperfections. Thus, for the future work, these experiments are to be repeated with cover slips and $\beta \sim 0.8$.

Earlier in this work we tried to perform experiments on 81 µm high channels (all having thick glass slides). The particle formed for all the cases discussed below, using thick slides were well defined since their heights were sufficient enough to make a clear distinction. We tried different oligomers with various photo-initiator concentrations: PEGDA 700, PEGDA 575 and PEGDA 250 with both 5% and 10% PI (v/v ratio), and with different lenses for photo-polymerization. Unfortunately, for both the PEGDA- 700/575, the particles when flown, either moved irregularly or got stuck within the channel after moving some distance (the toppled fibres estimated the particle confinements to be $\sim 0.8 - 0.85$ in all cases). This effect was more pronounced either when 10x lens was used for particle production, or for 5% concentration - even for 20x lens. We hypothesize that the particles formed are actually swelling up due to the diffusion of the medium surrounding it. The reason to eliminate the possibility of growing particles due to non-terminated radicals was because, the particles always got stuck only after travelling very small distances. If it were to continuously grow, then the waiting time before the start of the flow would actually make a difference, which indeed was not observed. The hypothesis made is also supported though the particle production using 10x lens. The depth of focus of 10x magnification is 30 µm (large when compared to 20x with 5 µm), and so the free radicals produced are well dispersed - enough to form a more porous polymer network.

From the above understanding of the setup we decided to go with PEDGA 250, with particles produced using 20x lens. However, in 81 µm channels we were unable to obtain smooth transition of the particles under flow. Thus we were left with no other choice other than choosing 33 µm heigh channels. The reason to choose 10% concentration was because the particles produced with the maximum available light intensity (ND1 scale in Nikon 130W UV lamp) were only $\beta \sim 0.7$ heigh. Thus PEDGA 250 with 10% (v/v ratio) PI concentration was used to produce and track particles in a 33 µm heigh channel with thick glass slide.

Bibliography

[1] W. B. Russel, D. A. Saville, and W. R. Schowalter. *Colloidal Dispersions*. Cambridge Monographs on Mechanics. Cambridge University Press, 1989. doi: 10.1017/CBO9780511608810.

[2] Sriram Ramaswamy. Issues in the statistical mechanics of steady sedimentation. *Advances in Physics*, 50(3):297–341, 2001. doi: 10.1080/00018730110050617. URL https://doi.org/10.1080/00018730110050617.

[3] Mehmet Toner and Daniel Irimia. Blood-on-a-chip. *Annual Review of Biomedical Engineering*, 7(1):77–103, 2005. doi: 10.1146/annurev.bioeng.7.011205.135108. URL https://doi.org/10.1146/annurev.bioeng.7.011205.135108. PMID: 16004567.

[4] Daniel R. Gossett, Westbrook M. Weaver, Albert J. Mach, Soojung Claire Hur, Henry Tat Kwong Tse, Wonhee Lee, Hamed Amini, and Dino Di Carlo. Label-free cell separation and sorting in microfluidic systems. *Analytical and Bioanalytical Chemistry*, 397(8):3249–3267, Aug 2010. ISSN 1618-2650. doi: 10.1007/s00216-010-3721-9. URL https://doi.org/10.1007/s00216-010-3721-9.

[5] George Whitesides. Whitesides, g.m. the origins and the future of microfluidics. nature 442, 368-373. *Nature*, 442:368–73, 08 2006. doi: 10.1038/nature05058.

[6] Shuo Sui and Sarah L. Perry. Microfluidics: From crystallization to serial time-resolved crystallography. *Structural Dynamics*, 4(3), 2017. ISSN 23297778. doi: 10.1063/1.4979640.

[7] Tsevi Beatus, Tsvi Tlusty, and Roy Bar-Ziv. Phonons in a one-dimensional microfluidic crystal. *Nature Physics*, 2(11):743–748, Oct 2006. ISSN 1745-2481. doi: 10.1038/nphys432. URL http://dx.doi.org/10.1038/nphys432.

[8] Yanan Liu, Brato Chakrabarti, David Saintillan, Anke Lindner, and Olivia du Roure. Morphological transitions of elastic filaments in shear flow. *Proceedings of the National Academy of Sciences*, 115(38):9438–9443, Sep 2018. ISSN 1091-6490. doi: 10.1073/pnas.1805399115. URL http://dx.doi.org/10.1073/pnas.1805399115.

[9] Howard Brenner John Happel. *Low Reynolds number hydrodynamics : with special applications to particulate media*. Springer; 1983 edition, 1983. ISBN 9024728770.

[10] Bianxiao Cui, Haim Diamant, and Binhua Lin. Screened hydrodynamic interaction in a narrow channel. *Physical review letters*, 89:188302, 11 2002. doi: 10.1103/PhysRevLett.89.188302.

[11] William E. Uspal, H Burak Eral, and Patrick S. Doyle. Engineering particle trajectories in microfluidic flows using particle shape. *Nature Communications*, 4(1):2666, dec 2013. ISSN 2041-1723. doi: 10.1038/ncomms3666. URL http://www.nature.com/articles/ncomms3666.

[12] H. Brenner. The Stokes resistance of an arbitrary particle. *Chemical Engineering Science*, 18(1):1–25, jan 1963. ISSN 00092509. doi: 10.1016/0009-2509(63)80001-9. URL https://linkinghub.elsevier.com/retrieve/pii/0009250963800019.

[13] H. Brenner. The Stokes resistance of an arbitrary particle-II. An extension. *Chemical Engineering Science*, 19(9):599–629, 1964. ISSN 00092509. doi: 10.1016/0009-2509(64)85051-X.

[14] Bram Bet, Rumen Georgiev, William Uspal, Huyesin Burak Eral, René van Roij, and Sela Samin. Calculating the motion of highly confined, arbitrary-shaped particles in Hele-Shaw channels. oct 2017. URL http://arxiv.org/abs/1710.04561.

[15] William E. Uspal and Patrick S. Doyle. Self-organizing microfluidic crystals. *Soft Matter*, 10(28):5177–5191, jun 2014. ISSN 1744-683X. doi: 10.1039/C4SM00664J. URL http://xlink.rsc.org/?DOI=C4SM00664J.

[16] Haim Diamant. Hydrodynamic interaction in confined geometries. *Journal of the Physical Society of Japan*, 78(4):1–13, 2009. ISSN 00319015. doi: 10.1143/JPSJ.78.041002.

[17] R. G. Cox and H. Brenner. Effect of finite boundaries on the Stokes resistance of an arbitrary particle. *Journal of Fluid Mechanics*, 28(02):391, 1967. ISSN 0022-1120. doi: 10.1017/s0022112067002150.

[18] R. G. Cox and H. Brenner. Effect of finite boundaries on the Stokes resistance of an arbitrary particle Part 2. *Journal of Fluid Mechanics*, 28(02):391, 1967. ISSN 0022-1120. doi: 10.1017/s0022112067002150.

[19] M. Nagel, P. T. Brun, H. Berthet, A. Lindner, F. Gallaire, and C. Duprat. Oscillations of confined fibres transported in microchannels. *Journal of Fluid Mechanics*, 2018. ISSN 14697645. doi: 10.1017/jfm.2017.662.

[20] Couette flow. https://nptel.ac.in/content/storage2/courses/112104118/lecture-26/26-1_couette_6low.htm.

[21] Henrik Bruus. Acoustofluidics 1: Governing equations in microfluidics. *Lab on a Chip*, 2011. ISSN 14730189. doi: 10.1039/c1lc20658c.

[22] Dhananjay Dendukuri, Priyadarshi Panda, Ramin Haghgooie, Ju Min Kim, T. Alan Hatton, and Patrick S. Doyle. Modeling of oxygen-inhibited free radical photopolymerization in a PDMS microfluidic device. *Macromolecules*, 41(22):8547–8556, 2008. ISSN 00249297. doi: 10.1021/ma801219w.

[23] Helene Berthet, Marc Fermigier, and Anke Lindner. Single fiber transport in a confined channel: Microfluidic experiments and numerical study. *Physics of Fluids*, 25(10), 2013. ISSN 10706631. doi: 10.1063/1.4823728.

[24] Rafael C. Gonzalez and Richard E. Woods. *Digital Image Processing (3rd Edition)*. Prentice-Hall, Inc., Upper Saddle River, NJ, USA, 2006. ISBN 013168728X.

[25] Bram Bet, Sela Samin, Rumen Georgiev, Huseyin Burak Eral, and René van Roij. Steering particles by breaking symmetries. *Journal of Physics: Condensed Matter*, 30(22):224002, jun 2018. ISSN 0953-8984. doi: 10.1088/1361-648X/aabea9. URL http://stacks.iop.org/0953-8984/30/i=22/a=224002?key=crossref.663fd8fede31ab09c7390f89b7b6e961.